machines

MDPI

Article

Optimization of a Photovoltaic Solar Water Pumping System Under Partial Shading Using Intelligent Algorithms: Applied to the Ecuadorian Coast Context

Rogger José Andrade-Cedeno [1,2,*], Jesús Alberto Pérez-Rodríguez [1,3], Victor Joel Pinargote-Bravo [4], Carlos David Amaya-Jaramillo [2], Yimy Jusseppy Zambrano-Zambrano [2], Josué Enmanuel Navarrete-Solano [2], Javier Antonio Rivadeneira-Mendoza [2] and Ciaddy Gina Rodríguez-Borges [3]

[1] Posgrado en Instrumentación, Facultad de Ciencias, Universidad Central de Venezuela, Caracas 1010, Venezuela; rogger.andrade@gmail.com (R.J.A.-C.); jesus.perez@gmail.com (J.A.P.-R.)
[2] Grupo de Investigación INIAC, Carrera de Electrónica y Automatización, Escuela Superior Politécnica Agropecuaria de Manabí Manuel Félix López, Calceta 130601, Ecuador; rjandrade@espam.edu.ec (R.J.A.-C.); carlos.amaya@espam.edu.ec (C.D.A.-J.); yjzambrano@espam.edu.ec (Y.J.Z.-Z.); jenavarrete@espam.edu.ec (J.E.N.-S.); jarivadeneira@espam.edu.ec (J.A.R.-M.)
[3] Grupo de Investigación ISII, Facultad de Ingeniería y Ciencias Aplicadas, Universidad Técnica de Manabí, Portoviejo 130101, Ecuador; jesus.perez@utm.edu.ec (J.A.P.-R.); ciaddy.rodriguez@utm.edu.ec (C.G.R.-B.)
[4] Grupo de Investigación SISCOM, Carrera de Computación, Escuela Superior Politécnica Agropecuaria de Manabí Manuel Félix López, Calceta 130601, Ecuador; vpinargote@espam.edu.ec
* Correspondence: rogger.andrade@gmail.com

Abstract

Photovoltaic solar water pumping systems (PVSWPS) offer a sustainable solution for water access in remote rural areas, but their performance depends on tracking the maximum power point (MPP) of the photovoltaic (PV) array, which partial shading complicates by creating multiple local maxima in the power–voltage curve. This study presents the design and simulation in MATLAB/Simulink of a complete PVSWPS (PV array, Ćuk DC–DC converter, permanent magnet DC motor–centrifugal pump and hydraulic network) under partial shading scenarios representative of the Ecuadorian coast. Three MPPT strategies were compared: incremental conductance (IC-MPPT), particle swarm optimization exploiting empirically identified voltage clusters (PSO-MPPT), and an artificial neural network trained on the irradiance-to-MPP voltage relationship (ANN-MPPT). IC-MPPT converged to a local maximum in three of five scenarios, with a mean tracking error of 20.45%, whereas PSO-MPPT and ANN-MPPT reached 0.65% and 1.14%, increasing the pumped volume by approximately 6.5% and 7.0% in five stepped scenarios and by 3.9% and 4.6% in a 60 s continuous irradiance profile. This came with a lower converter efficiency (84.25% for IC-MPPT vs. 80.11% and 79.52%), a trade-off between tracking accuracy and efficiency. The net gain in delivered water supports intelligent MPPT for PV water pumping under frequent partial shading.

Keywords: maximum power point tracking; partial shading condition; particle swarm optimization; artificial neural network; photovoltaic water pumping

Check for updates

Academic Editor: Farshid Naseri

Received: 3 September 2026
Revised: 28 October 2026
Accepted: 3 November 2026
Published: 8 November 2026

Copyright: © 2026 by the authors. Licensee MDPI, Basel, Switzerland. This article is an open access article distributed under the terms and conditions of the Creative Commons Attribution (CC BY) license.

1. Introduction

In the context of increasing global energy demand and the urgent need for sustainable energy solutions, photovoltaic (PV) systems have emerged as a viable alternative, particularly in remote and isolated regions where access to the electrical grid is limited [1–3]. The

Ecuadorian coast, characterized by its geographical diversity and dispersed rural communities, faces significant challenges in rural electrification, which may become more pronounced with the gradual reduction or removal of energy subsidies [4,5]. To address these challenges, the development of efficient and autonomous photovoltaic solar water pumping systems (PVSWPS) represents a promising approach for improving water accessibility, enhancing agricultural productivity, and supporting the socioeconomic development of rural communities [3,6,7].

Ecuador possesses significant photovoltaic energy potential, with annual global horizontal irradiance ranging from 2.8 to 6.4 kWh/m^2/day, exceeding the solar resource available in many European regions where photovoltaic technologies have been extensively deployed [5,8,9]. These favorable conditions make PVSWPS particularly attractive for rural and agricultural applications, offering a sustainable solution that reduces dependence on fossil fuels while contributing to the mitigation of greenhouse gas emissions and the reduction in the carbon footprint.

Solar water pumping systems convert solar energy into mechanical energy for water extraction and distribution, providing a clean, sustainable, and renewable alternative to conventional pumping systems powered by fossil fuels [1,4]. However, the overall performance of these systems strongly depends on their ability to operate near the maximum power point (MPP) of the photovoltaic (PV) array, which continuously varies with environmental conditions such as solar irradiance and cell temperature. Consequently, Maximum Power Point Tracking (MPPT) techniques play a crucial role in maximizing energy harvesting and improving system efficiency [6,7,10].

Among the various MPPT techniques reported in the literature, the Perturb and Observe (P&O) algorithm remains one of the most widely adopted due to its simplicity, low computational requirements, and ease of implementation [11–13]. Nevertheless, P&O-MPPT presents several limitations, particularly the persistent oscillations around the maximum power point (MPP) under steady-state conditions and reduced tracking performance under rapidly changing environmental conditions [1,14,15]. The Incremental Conductance (IC) algorithm has been proposed as an alternative to improve MPP tracking accuracy by exploiting the relationship between the instantaneous and incremental conductance of the photovoltaic (PV) array. Compared with P&OMPPT, IC-MPPT can provide more accurate MPP identification and reduce steady-state oscillations; however, its performance remains dependent on the perturbation step size and the accuracy of the measured electrical variables [16–18]. Several improved P&O-MPPT and IC-MPPT strategies have been proposed, including adaptive and variable step-size approaches, to achieve a better trade-off between convergence speed and steady-state oscillations [12,14,15,19].

These limitations become more significant under partial shading conditions (PSC), where the mismatch in solar irradiance among PV modules leads to multiple local maximum power points (LMPPs) in the P–V characteristic, while only one corresponds to the global maximum power point (GMPP). Conventional techniques such as P&O-MPPT and IC-MPPT may converge toward a local maximum and consequently fail to extract the maximum available power from the PV array [20–22].

Therefore, intelligent global optimization techniques have been investigated to improve GMPP tracking under PSC. Among them, Particle Swarm Optimization (PSO)-based MPPT algorithms have gained attention because of their global search capability and their ability to locate the GMPP in multimodal P–V characteristics [23–26]. However, PSO-MPPT performance may depend on the appropriate selection of algorithmic parameters and may involve additional computational complexity compared with conventional MPPT methods.

In addition to optimization-based approaches, Artificial Neural Network (ANN)-based MPPT techniques have emerged as intelligent alternatives for PV systems operating

under complex and rapidly varying conditions. ANNs can learn the nonlinear relationship between the operating conditions of the PV array and the corresponding MPP, enabling rapid estimation of the optimal operating voltage without requiring an exhaustive search of the P–V characteristic. Consequently, ANN-based MPPT approaches have attracted increasing attention for their potential to provide fast and accurate GMPP tracking under partial shading and varying environmental conditions [27–30].

Although numerous studies have investigated MPPT techniques for photovoltaic water pumping systems, limited research has focused on the comparative evaluation of conventional and intelligent MPPT strategies using system configurations representative of commercially available components in the Ecuadorian market and operating under environmental conditions characteristic of remote coastal regions of Ecuador. Consequently, the practical benefits of advanced MPPT techniques for locally deployable PVSWPS remain insufficiently explored.

To address this research gap, this study presents the design and simulation of a solar water pumping system for rural areas of the Ecuadorian coast. The proposed system incorporates a PV array, a Ćuk DC–DC converter, a DC motor–centrifugal pump assembly, and three MPPT strategies spanning conventional and intelligent approaches. The system is modeled and simulated in the Simulink/MATLAB R2022b environment using the specifications of commercially available components in the Ecuadorian market. The objective is to determine the most effective MPPT approach in terms of tracking efficiency, dynamic response, and operational stability under varying irradiance conditions. The main simulations are performed at a constant cell temperature of 25 °C in order to isolate the effect of partial shading. Because cell temperature shifts the voltage of the maximum power point, its influence on both the PSO and ANN strategies is evaluated separately in Section 4.8.

The use of MATLAB/Simulink-based modeling is supported by previous studies that have reported good agreement between simulation results and experimental measurements for photovoltaic systems and PV water pumping systems, demonstrating the capability of these models to accurately reproduce the electromechanical and dynamic behavior of the corresponding physical systems [31–33]. Therefore, a simulation-based approach is adopted in this study to evaluate the proposed system and compare the MPPT strategies under controlled and repeatable operating conditions.

To position the present work, Table 1 summarizes studies on MPPT for photovoltaic water pumping and, for reference, on intelligent MPPT in stand-alone PV systems related to this work. The table lists only what each paper states in its abstract and methods; where a feature is not reported, it is marked as not stated.

Table 1 shows three features of the previous work. First, studies on pumping under partial shading either compare metaheuristic algorithms, such as PSO and GWO, sometimes combined with a control technique such as one-cycle or sliding-mode control [34–36], or evaluate a single algorithm [13]. Second, among the works reviewed, only [37] compares the pumped water obtained with different algorithms under shading, and it compares an ANN with a scanning P&O, while [13] reports the instantaneous pump discharge under shading for P&O alone; the other pumping studies, including the ANN comparison in [28], rely on electrical indicators. Third, studies that include hybrid or intelligent algorithms under shading in non-pumping systems [23,38,39] do not include a motor–pump–pipe model, so they cannot show how the tracked power becomes water.

Accordingly, the contribution of this work is not a new MPPT algorithm but a comparison under one electro-hydraulic model, in four parts: (i) a complete photovoltaic water pumping model built from commercially available components in Ecuador; (ii) the evaluation under partial shading of three strategies, a conventional IC, a PSO that uses the cluster structure of the GMPP voltage found in a 1000-scenario dataset, and an ANN that estimates

the GMPP voltage from irradiance, in the same Ćuk-fed PMDC motor–centrifugal pump–pipe model; (iii) the report of pumped volume together with the energy at each stage (PV array, converter output, motor shaft, hydraulic output), which separates converter, motor, and pump efficiencies and shows that the extra water pumped by PSO and ANN comes with a lower converter efficiency; and (iv) the comparison of the sensing requirements of each strategy. These conclusions come from simulation, five irradiance scenarios, and a 20 s window, and they are limited to the conditions evaluated.

Table 1. Studies on MPPT under partial shading (PV water pumping and related systems) compared with this work.

Ref.	Application	Converter/Motor and Pump	MPPT Algorithms	Pumped Volume Reported
Pant and Saini, 2020 [13]	PV water pumping	Boost; PMDC motor, centrifugal pump	P&O only	Instantaneous discharge only (L/s)
Nisha and Gnana Sheela, 2022 [34]	PV water pumping	KY converter + VSI; BLDC motor pump	Cuckoo search, PSO, GWO with one-cycle control	Not stated
Khadija et al., 2023 [35]	PV water pumping	Boost + inverter; BLDC centrifugal pump	PSO, GWO with sliding-mode control	Not stated
Merbah and Tadjer, 2026 [36]	PV water pumping	DC–DC; BLDC motor pump	P&O, PSO, GWO, marine predator	Not stated
Bouselham et al., 2016 [37]	PV water pumping	Boost; DC motor, centrifugal pump	ANN with P–V scanning vs. variable-step P&O with global scanning	Yes
BalaKumar et al., 2025 [28]	PV pumping for irrigation	Zeta + VSI; BLDC motor, positive-displacement pump	ANN vs. P&O (shading not stated)	Not stated
Hayder et al., 2022 [38]	Stand-alone PV, DC load (no pumping)	Boost	Improved PSO, neural-network P&O	Not applicable
Cruz et al., 2025 [39]	Stand-alone PV (no pumping)	Boost	ANN + P&O hybrid vs. P&O, differential evolution	Not applicable
Al-Muthanna et al., 2023 [23]	PV battery charging (no pumping)	Boost	Hybrid PSO-PID vs. PSO, bat algorithm	Not applicable
This work	PV pumping with electro-hydraulic model	Ćuk converter, PMDC motor, centrifugal pump, pipe network	IC, PSO (cluster prior, event-triggered), ANN (irradiance inputs)	Yes, with energy at each stage

2. System Modeling and Simulation

The proposed photovoltaic solar water pumping system (PVSWPS) consists of five main subsystems: a photovoltaic (PV) array, a Ćuk DC–DC converter, a DC motor-driven centrifugal pump, a PI controller, and an MPPT algorithm, as illustrated in Figure 1. The PV array serves as the primary energy source, converting solar radiation into electrical power. To maximize energy extraction from the PV array, a Maximum Power Point Tracking (MPPT) algorithm is employed. Three MPPT strategies are evaluated in this study, comprising both conventional and intelligent approaches. The conventional category includes the Incremental Conductance (IC-MPPT) algorithm, while the intelligent category comprises

Particle Swarm Optimization (PSO-MPPT) and Artificial Neural Network (ANN-MPPT) algorithms. These strategies are comparatively evaluated to assess their effectiveness in tracking the maximum power point of the photovoltaic (PV) array under varying operating conditions, including partial shading conditions (PSC).

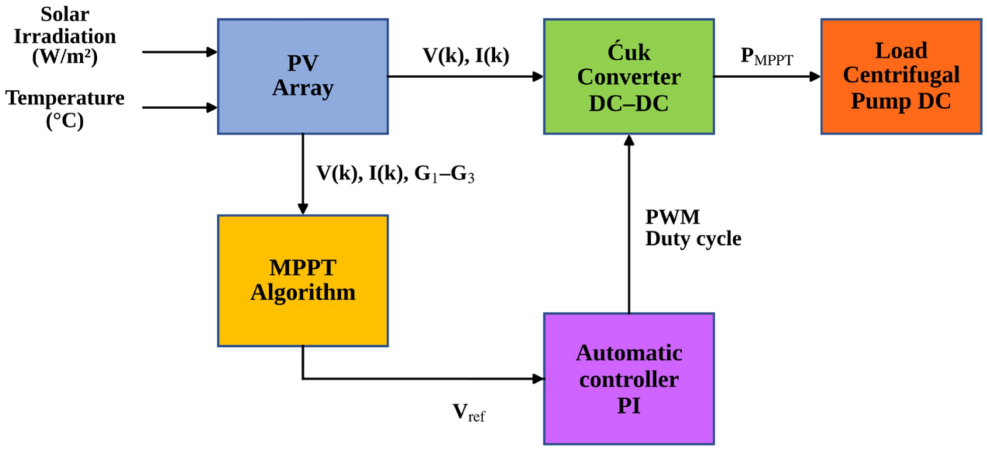


Figure 1. Schematic of the proposed photovoltaic water-pumping system. A PV array supplies a DC motor, via a Ćuk DC–DC converter, that drives a centrifugal pump. The MPPT algorithm (IC, PSO or ANN) generates the reference voltage Vref, which a PI voltage controller regulates by setting the PWM duty cycle of the converter.

The power generated by the PV array is processed through a Ćuk DC–DC converter, which regulates the voltage and current supplied to the motor. The converter was selected because of its ability to provide either step-up or step-down voltage conversion while maintaining continuous input and output currents, thereby improving system stability and reducing current ripple. The electromechanical subsystem consists of a DC motor mechanically coupled to a centrifugal pump. The motor converts electrical energy into mechanical energy, which is subsequently transferred to the pump for water delivery. A PI voltage controller regulates the PV array voltage at the reference set by the MPPT algorithm, which keeps the pump operating under varying environmental conditions. A complete model of the proposed PVSWPS was developed in the Simulink/MATLAB R2022b environment, as shown in Figure 2.

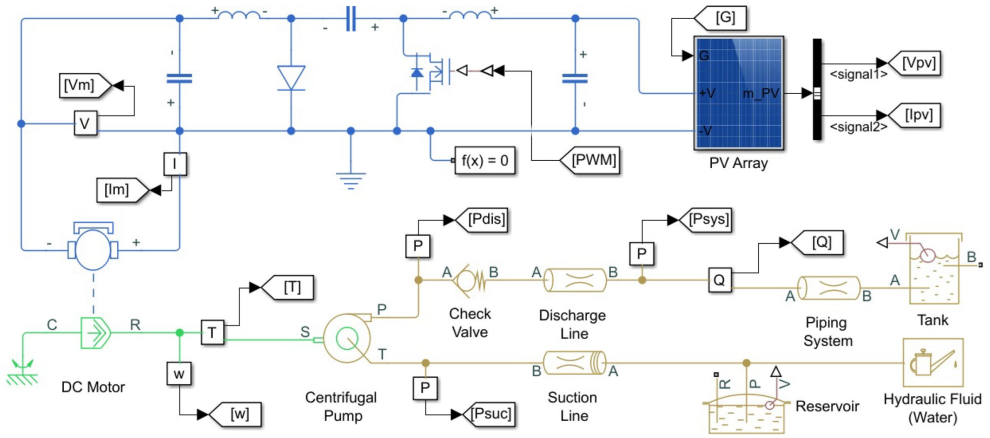


Figure 2. The global model in Figure 2 was built with one block per subsystem; the relationships used for each are summarized in Table 2. Blue lines represent electrical connections, green lines mechanical connections and brown lines hydraulic connections.

Table 2. Subsystems of the global model in Figure 2 and the relationships used to model them.

Subsystem (Figure 2)	Model and Implementation	Equations	Section
PV array	Two-diode cell model	Equations (1) and (2)	Section 2.1
Ćuk converter	CCM and DCM steady-state relations; component sizing	Equations (3)–(15)	Section 2.2
PMDC motor	Armature circuit and mechanical equations	Equations (16)–(21)	Section 2.3
Centrifugal pump	Affinity laws from manufacturer data	Equations (22)–(27)	Section 2.4
Hydraulic network	Head-loss, friction-factor and Reynolds-number relations	Equations (28)–(30)	Section 2.5
PI controller	Discrete incremental PI	Equation (31)	Section 3.1
MPPT algorithm	IC, PSO and ANN-MPPT	-	Sections 3.2–3.4

Each block of Figure 2 is defined by the relationships given in this section and in Section 3, and Table 2 links every block to its model.

2.1. Photovoltaic Array

The proposed PV array was developed using a hierarchical modeling approach based on individual photovoltaic (PV) cells. PV cells convert solar radiation into direct-current (DC) electrical energy through the photovoltaic effect. This phenomenon occurs when incident photons with sufficient energy generate electron–hole pairs within the semiconductor material, which are subsequently separated by the electric field of the p–n junction, producing an electric current [40].

Each PV cell was modeled using the Solar Cell block available in the Simscape Electrical library of MATLAB/Simulink. The block represents the electrical behavior of a PV cell through an equivalent circuit comprising a photogenerated-current source, two diodes, a series resistance, and a parallel resistance [41–43]. This model captures the nonlinear current–voltage behavior of the PV cell and its dependence on solar irradiance and temperature.

The PV cell was modeled using the equivalent circuit shown in Figure 3, whose mathematical formulation is given by:

$$I = I_{ph} - I_{s1}\cdot\left(e^{\frac{(V+I\cdot R_s)}{(N_1\cdot V_T)}} - 1\right) - I_{s2}\cdot\left(e^{\frac{(V+I\cdot R_s)}{(N_2\cdot V_T)}} - 1\right) - (V + I\cdot R_s)/R_p \quad (1)$$

where I is the output current of the PV cell, I_{ph} is the photogenerated current, I_{s1} and I_{s2} are the saturation currents of both diodes, V_T is the thermal voltage, defined as kT/q, where k is the Boltzmann constant, T is the device temperature, and q is the elementary charge; N_1 and N_2 are the quality factors (diode emission coefficients) of both diodes, R_s and R_p are the series and shunt resistances, respectively; and V is the voltage across the electrical terminals of the PV cell. The quality factor depends on the semiconductor technology. This formulation allows the electrical response of the PV cell to be represented under different irradiance and temperature conditions.

The Solar Cell block also allows multiple series-connected cells to be represented within a single block by specifying the number of cells connected in series. In the proposed model, this capability was used to represent each 24-cell block. Three such blocks were then connected in series, with each block protected by a bypass diode, to reproduce the electrical topology of the PV panels considered in this study.

For this research, each PV cell was characterized by a short-circuit current of 13 A, an open-circuit voltage of 0.65 V, and a series resistance of 0.01 Ω. These cell parameters are defined at a measurement temperature of 25 °C, while the simulation temperature is set separately; the temperature coefficient of the photogenerated current is set to zero, so a change in cell temperature affects the cell voltage but not its short-circuit current. Each

PV panel was represented by three series-connected blocks, with each block comprising 24 series-connected PV cells and protected by a bypass diode. Each PV panel therefore consists of 72 series-connected PV cells, exhibits an open-circuit voltage of approximately 46.8 V, and maintains a short-circuit current of 13 A. Two PV panels were then connected in series to form a photovoltaic (PV) string, resulting in a total of 144 series-connected PV cells per string, an open-circuit voltage of approximately 93.6 V, and a short-circuit current of 13 A. The complete PV array is composed of four parallel PV strings, providing an overall open-circuit voltage of approximately 93.6 V and a short-circuit current of 52 A. The complete architecture of the proposed PV array is illustrated in Figure 4.

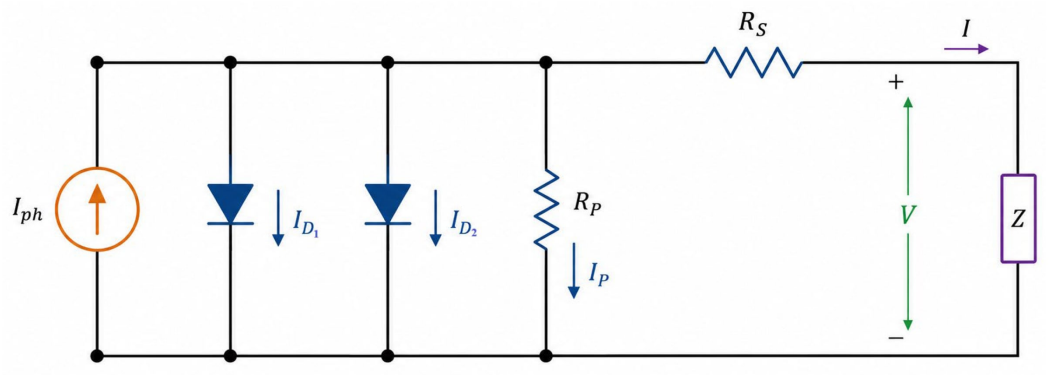


Figure 3. Equivalent circuit of a PV cell comprising a photogenerated current source I_{ph}, diode D_1, diode D_2, series resistance R_s, parallel resistance R_p, and output voltage V.

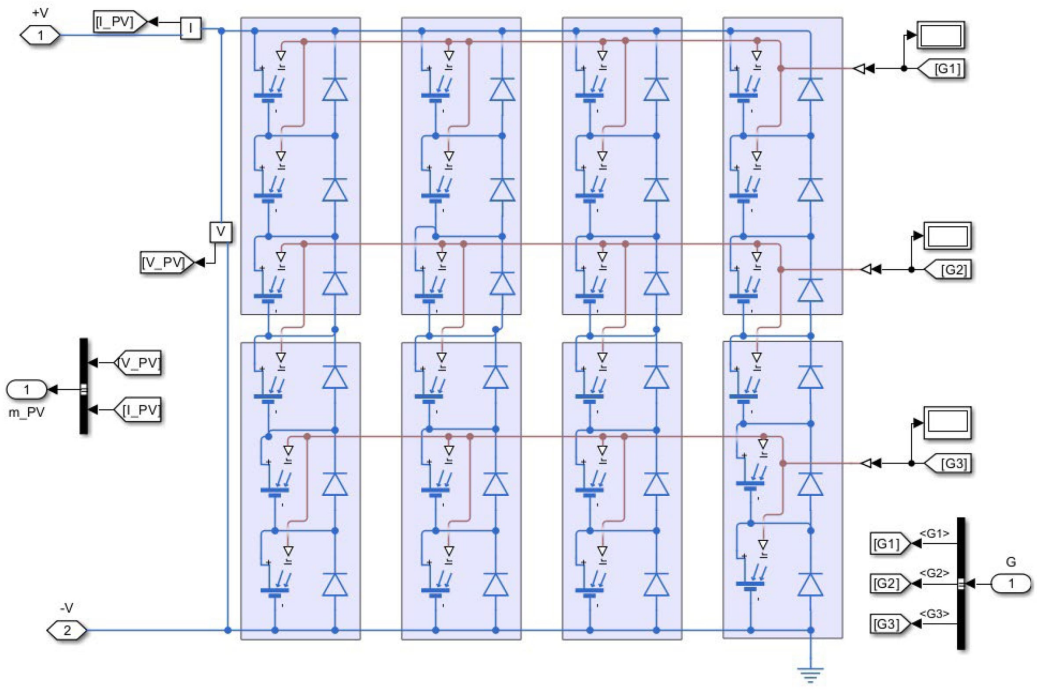


Figure 4. Proposed photovoltaic (PV) array configuration: four parallel strings, each formed by two series-connected PV panels. Each panel has three series-connected 24-cell blocks, each protected by a bypass diode. The irradiance signals G_1, G_2 and G_3 each act on two series-connected blocks of every string.

To characterize the electrical performance of PV panels, manufacturers provide technical specifications measured under Standard Test Conditions (STC), defined as a solar irradiance of 1000 W/m^2, a cell temperature of 25 °C, and an air mass of AM 1.5 G. These specifications typically include the short-circuit current (I_{SC}), open-circuit voltage (V_{OC}), maximum power (P_{MAX}), and the voltage and current at the maximum power point (V_{MP} and I_{MP}) [44,45]. Such parameters are essential for accurate modeling, analysis, and sizing of photovoltaic systems in practical applications.

The electrical power delivered by the PV array is obtained from the product of its output voltage and current and can be expressed as:

$$P_{pv} = V_{pv} \cdot I_{pv} \tag{2}$$

where P_{pv} is the total power produced by the PV array, and V_{pv} and I_{pv} are its output voltage and current, respectively. The resulting I–V and P–V characteristic curves provide a comprehensive description of the PV array behavior under different environmental operating conditions.

The mathematical model described by Equations (1) and (2) was used to generate the current–voltage (I–V) and power–voltage (P–V) characteristic curves of the PV array under different operating conditions, as shown in Figure 5. These curves provide valuable insight into the electrical behavior of the PV array and its response to variations in solar irradiance and cell temperature. The I–V characteristic illustrates the nonlinear relationship between the output current and voltage, whereas the P–V characteristic identifies the operating point at which the maximum power is extracted from the PV array [32,46,47]. As irradiance and temperature vary, both curves shift, causing changes in the location of the MPP. Therefore, accurate representation of these characteristics is essential for the design and evaluation of MPPT algorithms.

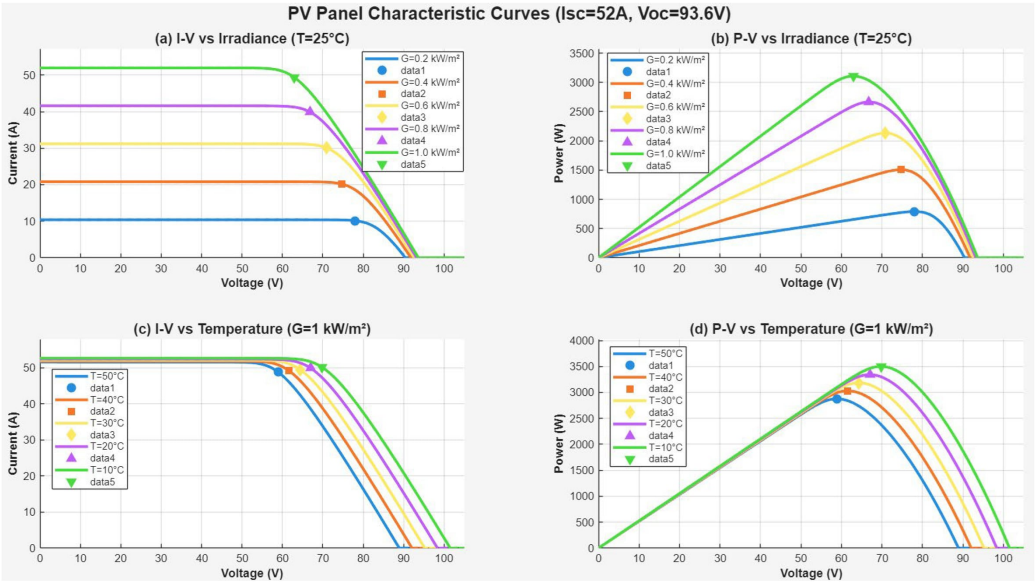


Figure 5. I–V and P–V characteristic curves of the simulated PV array under varying irradiance levels (0.3–1 kW/m^2) and cell temperatures (10–35 °C). (**a**,**b**) Curves obtained at a fixed cell temperature of 25 °C while sweeping irradiance. (**c**,**d**) Curves obtained at a fixed irradiance of 1 kW/m^2 while sweeping cell temperature.

Cell temperature also affects the power–voltage characteristic of the PV array. The Ecuadorian coastal region has an annual mean ambient temperature between 24 °C and 26 °C, but cells in operation are typically 20–30 °C above ambient under high insolation,

so the cell temperature can be well above the temperature at which the cell parameters are defined (25 °C). With a typical temperature coefficient of the open-circuit voltage of approximately −0.3 to −0.5%/°C, this shifts the GMPP voltage by several volts (Section 4.8).

Partial shading conditions (PSCs) are incorporated into the PV array model by assigning three irradiance levels, G_1, G_2 and G_3, to groups of two series-connected 24-cell blocks, as illustrated in Figure 4: G_1 acts on the first two blocks of the upper panel, G_2 on the last block of the upper panel and the first block of the lower panel, and G_3 on the last two blocks of the lower panel. The same assignment is applied to the four parallel strings.

Under uniform irradiance conditions, all blocks receive the same irradiance level. In contrast, partial shading conditions are represented by non-uniform irradiance distributions in which different groups of blocks receive different irradiance levels. These irradiance mismatches cause differences in the current generated by the affected blocks and modify the overall P–V characteristic of the PV array.

Due to the series connection of the cell blocks and the operation of the bypass diodes, non-uniform irradiance can cause multiple peaks to appear in the P–V characteristic of the PV array. The highest peak corresponds to the global maximum power point (GMPP), while the remaining peaks correspond to local maximum power points (LMPPs). Therefore, under partial shading conditions, conventional local search techniques may converge to an LMPP instead of the GMPP [20,23,41].

The proposed PV array configuration allows different partial shading patterns to be reproduced by independently varying G_1, G_2 and G_3, while maintaining the same electrical topology. Each irradiance distribution represents a specific operating condition of the PV array and produces a corresponding P–V characteristic with a distinct GMPP. For each condition, the voltage associated with the GMPP is identified from the resulting P–V characteristic. This voltage represents the optimal operating point at which the PV array delivers its maximum available power under the corresponding irradiance distribution [20,23,41]. Applying the same irradiance triplet to the four strings was a modeling choice that yields controlled and reproducible multimodal P–V curves with only three independent irradiance variables; independent shading of each string or module is not considered and is listed as a limitation in Section 5.

The resulting relationship between the irradiance distribution and the GMPP voltage provides the reference information required to train the proposed ANN-based MPPT algorithm.

2.2. Ćuk DC–DC Converter

The Ćuk converter was selected as the power-conditioning stage of the PVSWPS for its non-isolated buck-boost operating principle, which allows the output voltage to be either lower or higher than the input voltage depending on the duty cycle, while maintaining continuous input and output currents—reducing ripple and filtering requirements in photovoltaic applications [48–50]. Figure 6 shows its electrical configuration: an energy-transfer capacitor together with input and output inductors transfers energy from source to load; as with all non-isolated Ćuk topologies, the output voltage polarity is inverted relative to the input.

By modulating the duty cycle via PWM, the converter regulates the PV array's operating point, driving it toward the MPP identified by the MPPT controller—acting simultaneously as the voltage-adaptation interface between the PV array and the motor–pump subsystem and as the power-processing stage through which MPPT is implemented [51]. The converter was modeled in both continuous (CCM) and discontinuous (DCM) conduction modes to represent its behavior across the full operating range, including the low-irradiance

conditions that may occur during partial shading. Under ideal CCM, the steady-state voltage conversion ratio is given by:

$$V_o/V_{in} = -D/(1-D) \tag{3}$$

where V_o, V_{in}, and D are the output voltage, input voltage, and duty cycle, respectively; the negative sign reflects the polarity inversion of the Ćuk topology. Equations (4)–(10) describe the relationships among duty cycle, switching frequency, and passive components under CCM, used to size the required inductors and capacitors and to verify current and voltage ripple:

$$V_{C2} = -V_o \tag{4}$$

$$D = V_o/(V_o + V_{in}) \tag{5}$$

$$T = 1/f \tag{6}$$

$$L_{1_{min}} = \left(R\cdot(1-D)^2\right)/(2\cdot D\cdot f) \tag{7}$$

$$L_{2min} = \left(R\cdot(1-D)^2\right)/(2\cdot f) \tag{8}$$

$$C_2 \geq (1-D)/\left(8\cdot L_2\cdot f^2\cdot(\Delta V_O/V_O)\right) \tag{9}$$

$$C_1 \geq (D\cdot V_O)/(f\cdot\Delta V_{C1}\cdot R) \tag{10}$$

where D, f, T, L_1, L_2, C_1, C_2, R, V_{in}, V_o, I_{L0}, ΔV_{C1}, and ΔV_{C2} are the duty cycle, switching frequency, switching period, input/output inductors, coupling/output capacitors, load resistance, converter input/output voltage, discontinuous-mode inductor current, and the voltage ripples across C_1 and C_2, respectively.

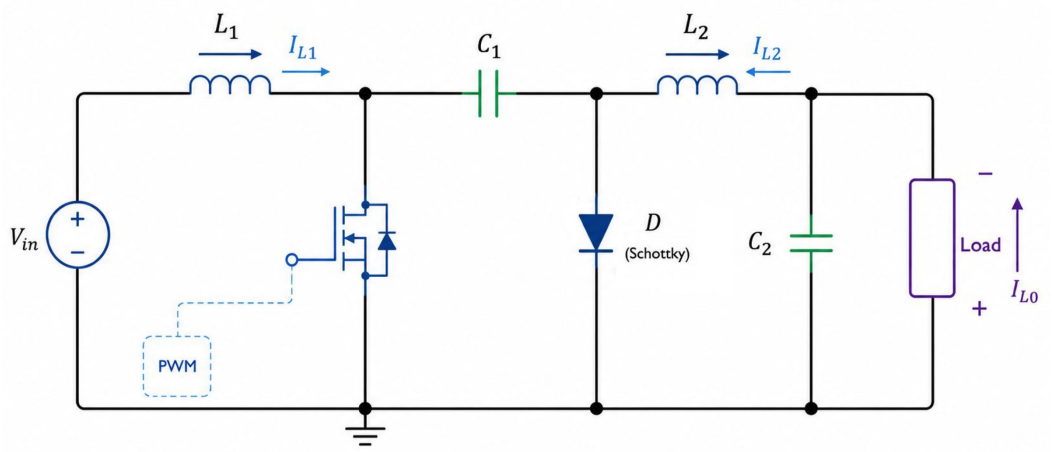


Figure 6. Electrical schematic of the Ćuk DC–DC converter showing the input inductor L_1, energy-transfer capacitor C_1, output inductor L_2, output capacitor C_2, MOSFET switching device, Schottky diode D, and load.

When one or both inductor currents become discontinuous, the converter operates in DCM, whose steady-state relationships (Equations (11)–(15)) were used to characterize the converter's operating limits and verify its behavior under low-power conditions:

$$I_{L0} = 0.5\cdot(V_{in}\cdot DT\cdot((D/L_2) - (\propto/L_1))) \tag{11}$$

$$\propto = \sqrt{(2\cdot L_{12})/(R\cdot T)} \tag{12}$$

$$L_{12} = (L_1\cdot L_2)/(L_1 + L_2) \tag{13}$$

$$\Delta V_{C1} = \frac{D\cdot T\cdot\Delta I_{L2}}{2\cdot C_1}\cdot\left(\frac{\Delta I_{L2} - I_{L0}}{\Delta I_{L2}}\right)^2 \tag{14}$$

$$\Delta V_{C2} = \frac{((D+\propto)\cdot T\cdot \Delta I_{L2})}{2\cdot C_2}\cdot\left(\frac{\Delta I_{L2} - I_{L0} - I_0}{\Delta I_{L2}}\right)^2 \quad (15)$$

The passive components were sized accordingly, and the resulting model was integrated with the PV array, MPPT controller, and motor–pump subsystem in MATLAB/Simulink R2022b. The converter uses $L_1 = 1$ mH, $C_1 = 150$ µF, $L_2 = 2$ mH and $C_2 = 560$ µF, with a 2.2 mF capacitor at the PV array terminals. Since the PV array delivers an open-circuit voltage of approximately 93.6 V (Section 2.1) while the PMDC motor is rated at 200 V, the converter operates mainly in boost mode; from Equation (5), $D = 200/(200 + 93.6) \approx 0.68$ at nominal conditions; during the simulations the duty cycle ranged from about 0.56 to 0.90, and the converter remained in CCM in steady state.

2.3. Permanent Magnet DC Motor

The electromechanical conversion stage is performed by a 200 V, 4 kW, 3500 rpm permanent magnet DC (PMDC) motor mechanically coupled to a centrifugal pump, with the complete motor–pump subsystem implemented in Simscape Electrical and Simscape Fluids. In a PMDC motor, the constant magnetic flux from stator-mounted permanent magnets yields fixed back-EMF and torque constants [52], simplifying the model while preserving an accurate representation of the electromechanical dynamics. The motor was implemented using the DC Machine block (Simscape Electrical, permanent-magnet mode); its armature circuit comprises inductance L_a and resistance R_a in series with the back-EMF EE, proportional to rotor angular speed [52–54], as shown in Figure 7.

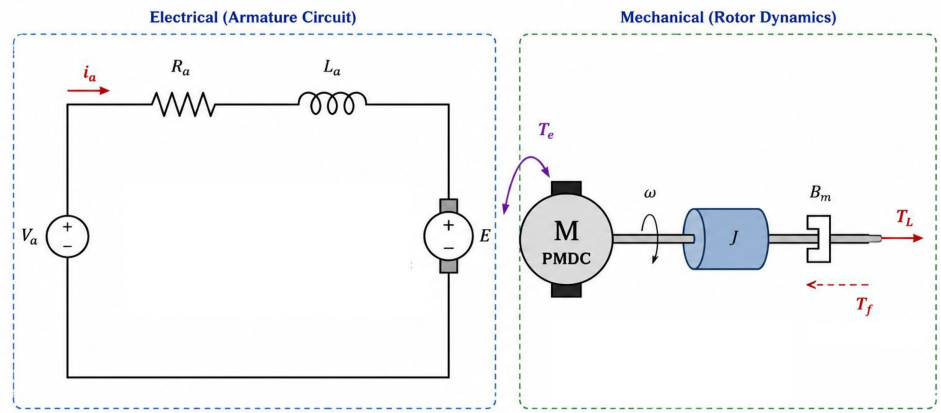


Figure 7. Equivalent model of the permanent magnet DC motor (PMDC).

The PMDC motor model is described by Equations (16)–(20):

$$V_a = R_a\cdot i_a + L_a\cdot(di_a/dt) + E \quad (16)$$

$$E = K_E\cdot\omega \quad (17)$$

$$T_e = K_T\cdot i_a \quad (18)$$

$$K_T = K_E \quad (19)$$

$$J\cdot(d\omega/dt) = T_e - T_L - (B_m\cdot\omega) - T_f \quad (20)$$

where V_a, i_a, R_a, L_a, E, K_E, ω, T_e, K_T, J, T_L, B_m, and T_f are the armature voltage, armature current, armature resistance, armature inductance, back-EMF, back-EMF constant, angular velocity, electromagnetic torque, torque constant, combined motor–pump moment of inertia, pump load torque, viscous friction coefficient, and Coulomb friction torque, respectively.

Under steady-state conditions ($di_a/dt \approx 0$), substituting Equation (17) into Equation (16) gives the armature-voltage/speed relationship:

$$\omega = (V_a - R_a i_a)/K_E \tag{21}$$

Figure 8 shows the resulting speed–torque characteristics: as armature voltage decreases, no-load and loaded speed decrease proportionally while the speed–torque relationship remains approximately linear [55], with the motor's operating point set by the intersection of its own speed–torque characteristic and the load torque imposed by the centrifugal pump.

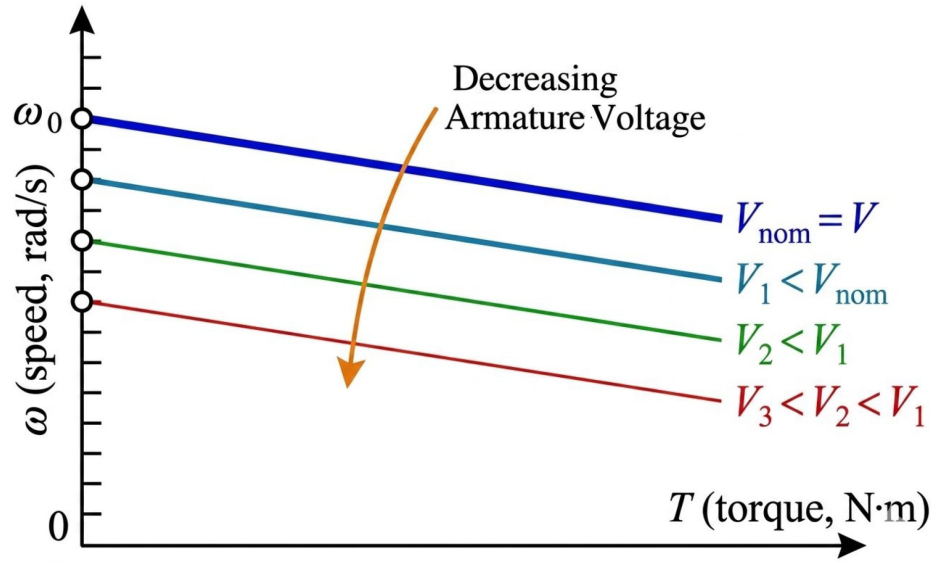


Figure 8. Torque–speed characteristics of the permanent magnet DC motor under different armature voltages. The curves illustrate the reduction in steady-state motor speed as the armature voltage decreases, while maintaining an approximately linear relationship between speed and load torque.

Together, Equations (16)–(21) link the armature circuit's electrical variables to the rotor's mechanical variables, establishing the relationship between the PV-supplied electrical power and the pump-delivered mechanical power, with the Ćuk converter acting as the actuator that regulates motor speed via armature-voltage control. This model was integrated with the PV array, the Ćuk converter, the MPPT controller, and the hydraulic subsystem for full-system evaluation.

2.4. Centrifugal Pump

The centrifugal pump converts the DC motor's mechanical energy into hydraulic energy [56], implemented in Simscape Fluids and mechanically coupled to the motor shaft; it receives angular velocity ω and torque T as inputs and outputs the hydraulic flow rate q and pressure increase Δp [4].

Pump parameters were configured from manufacturer data at rated conditions (120 gpm flow, 35 m head, 3500 rpm), defining the reference operating point for the head–flow and power–flow curves at nominal speed and fluid density [4,56]. Performance under other conditions was predicted using the affinity laws [57]: flow rate scales linearly with rotational speed, while pressure and hydraulic power scale with the square and cube of the speed ratio, respectively, as expressed by Equations (22)–(27):

$$q = q_{nom} \cdot (\omega/\omega_{nom}) \tag{22}$$

$$\Delta p = \Delta p_{nom} \cdot (\omega/\omega_{nom})^2 \cdot (\rho/\rho_{nom}) \tag{23}$$

$$P_{hyd_nom} = \Delta p_{nom} \cdot q_{nom} \tag{24}$$

$$P_{hyd} = P_{hyd_nom} \cdot (\omega/\omega_{nom})^3 \cdot (\rho/\rho_{nom}) \tag{25}$$

$$P_{mec} = T\omega \tag{26}$$

$$\eta = P_{hyd}/P_{mec} \tag{27}$$

where q, Δp, ω, T, ρ, P_{hyd}, P_{mec}, and η are the volumetric flow rate, pressure increase, shaft angular velocity, motor torque, fluid density, hydraulic power, mechanical shaft power, and pump efficiency, respectively; the subscript *nom* denotes nominal manufacturer conditions.

Figure 9 shows the resulting head–flow and power curves at different shaft speeds, together with the hydraulic system curve and iso-efficiency lines: increasing rotational speed shifts the pump curves upward, yielding higher flow rates and developed head, with the operating point set by the intersection of the pump and system curves [56,58]. Since motor speed variations directly affect flow rate, pressure, hydraulic power, and pumping efficiency, and the available PV power varies continuously with solar irradiance, the Ćuk converter automatically adjusts the pump's operating point to the available photovoltaic power—maximizing water delivery while maintaining efficient operation.

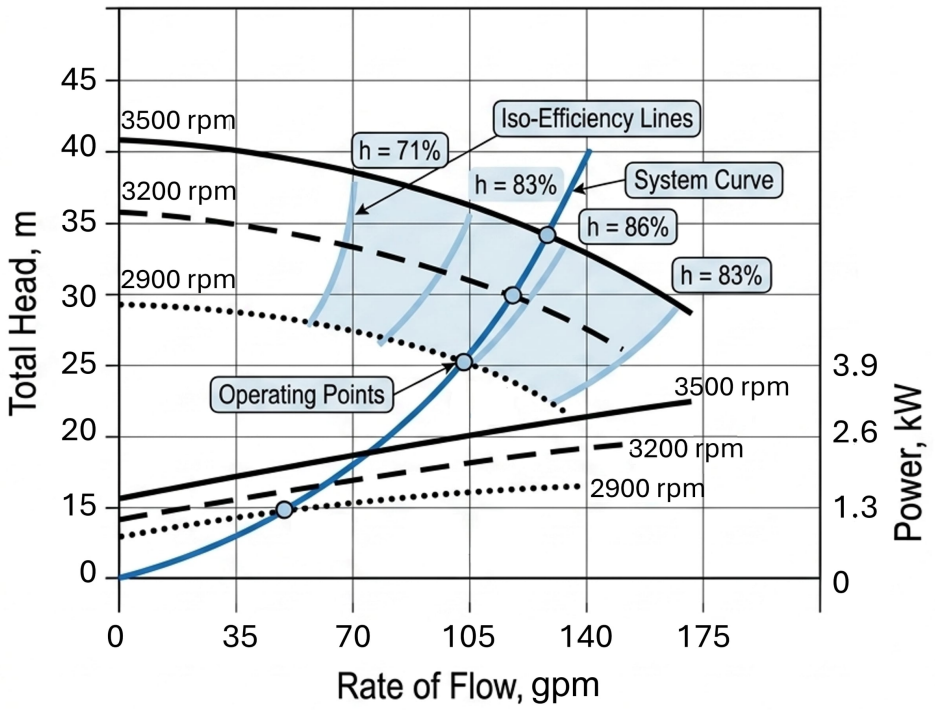


Figure 9. Performance curves of the centrifugal pump at different rotational speeds.

2.5. Hydraulic Pip System

The hydraulic network—a suction line, a discharge line, and a main delivery pipeline—was implemented using Simscape Pipe blocks in MATLAB/Simulink R2022b, interconnected with the centrifugal pump and storage tank to reproduce the dynamic behavior of water transport. Only major losses caused by pipe-wall friction were considered; minor losses from fittings, valves, and accessories were neglected. Pressure losses along each pipe section were calculated using the Darcy–Weisbach equation, relating pressure drop to pipe geometry, fluid properties, and flow conditions [59]. The friction factor was estimated using the Haaland approximation under turbulent flow, with linear interpolation

in the laminar-turbulent transition region. The resulting pressure-loss model is expressed by Equations (28)–(30).

$$p = f\frac{(L + Leq)}{D_H}\cdot\frac{\rho}{2A^2}\cdot q\cdot|q| \tag{28}$$

$$f = \begin{Bmatrix} K_s/R_e & if\ Re \le Re_L \\ f_L + \frac{(f_T - f_L)}{(Re_T - Re_L)}\cdot(Re - Re_L) & if\ Re_L \le Re < Re_T \\ \frac{1}{\left(-1.8\ Log\ 10\cdot\left(\frac{6.9}{Re} + \left(\frac{r/D_H}{3.7}\right)^{1.11}\right)\right)^2} & if\ Re \ge Re_T \end{Bmatrix} \tag{29}$$

$$Re = \frac{q\cdot D_H}{A\cdot v} \tag{30}$$

where p, f, L, L_{eq}, D_H, ρ, A, q, Re, v, and r are the pressure drop, Darcy friction factor, pipe length, equivalent hydraulic-loss length, hydraulic diameter, fluid density, pipe cross-sectional area, volumetric flow rate, Reynolds number, kinematic viscosity, and internal pipe roughness, respectively.

The suction-line model also allows the elevation of ports A and B to be specified, enabling simulation of installations where the pump operates below the water source—such as wells, reservoirs, or underground cisterns. Incorporating both hydraulic losses and elevation effects provides a realistic representation of the hydraulic load imposed on the pump under different operating conditions.

3. Conventional and Intelligent Algorithms

3.1. Voltage Regulator PI Algorithm

Figure 10 illustrates the automatic control scheme implemented for the DC–DC converter voltage regulator of the photovoltaic (PV) system.

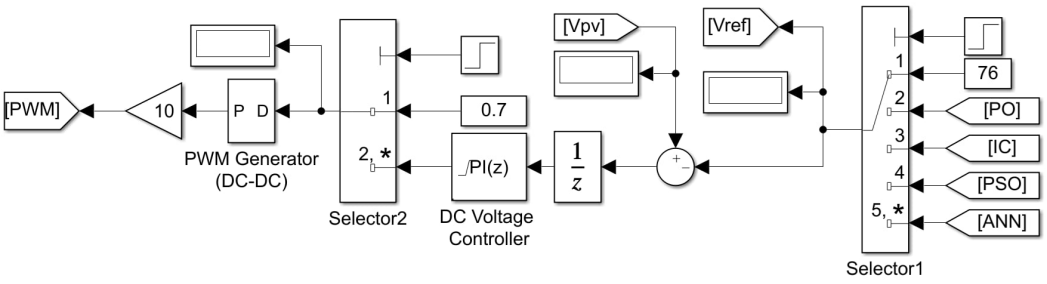


Figure 10. Control scheme of the DC–DC converter for PV array voltage regulation. The selector chooses the reference voltage V_{ref} from the MPPT algorithm under test (IC, PSO or ANN) or from a manual value used for testing; V_{ref} is compared with the measured PV voltage V_{pv}, and a discrete PI controller sets the duty cycle of the PWM generator.

The objective of the controller is to regulate the PV array voltage (V_{PV}) around the maximum power point (MPP), thereby ensuring efficient energy extraction under varying irradiance conditions. To achieve this, the measured PV array voltage (V_{PV}) is compared with the reference voltage (V_{ref}), generating the error signal e. This reference voltage (V_{ref}) constitutes the set point of the PI controller and is supplied, in each simulation, by the MPPT algorithm under evaluation—that is, alternately by the IC-MPPT [19,60], PSO-MPPT [23,26], or ANN-MPPT [61,62] algorithm described in Sections 3.2–3.4. Since the same voltage-regulation loop is used regardless of which MPPT strategy provides the set point, the PI controller itself remains fixed across all tests, ensuring that any difference in system performance can be attributed to the MPPT algorithm rather than to the underlying voltage

control loop. This error is processed by a discrete PI controller [63], whose incremental control law is given by:

$$u(z) = K_p \cdot e(z) + K_i \cdot \left[\frac{T_s}{z-1}\right] \cdot e(z) \tag{31}$$

where $u[z]$ is the control signal, $e[z] = V_{ref}[z] - V_{PV}[z]$ is the voltage error, K_p and K_i denote the proportional and integral gains, respectively, and T_s is the controller sampling period. The output of the PI controller is used to generate the PWM signal that drives the switching of the DC–DC converter, thereby regulating the PV array voltage at the value set by the MPPT algorithm, V_{ref}. In all simulations, $K_p = 0.2$, $K_i = 10$ and $T_s = 100$ µs, equal to the switching period of the PWM modulator ($f_{sw} = 10$ kHz), so the duty cycle is updated once per switching period. The same controller parameters were used for the three MPPT strategies and for all scenarios, so the comparison is not affected by controller retuning.

3.2. Conventional MPPT Algorithms

Among the various MPPT strategies reported in the literature, the Perturb and Observe (P&O) and Incremental Conductance (IC) algorithms remain the two most widely adopted in commercial applications, owing to their simplicity and straightforward sensing requirements [11,12,64]. P&O is described here as the theoretical basis of IC-MPPT; only IC-MPPT is simulated as the conventional baseline in this work.

The conventional Perturb and Observe (P&O) algorithm periodically measures the PV array voltage $V(k)$ and current $I(k)$ to estimate the instantaneous output power $P(k) = V(k) \cdot I(k)$. At each sampling instant k, the algorithm evaluates the variations in power and voltage relative to the previous instant,

$$\Delta P(k) = P(k) - P(k-1), \qquad \Delta V(k) = V(k) - V(k-1) \tag{32}$$

and updates the reference voltage V_{ref} according to the sign of the power–voltage sensitivity $\Delta P(k) \cdot \Delta V(k)$

$$V_{ref} = \begin{cases} V_{ref}(k) + \Delta V_{step}, & \Delta P(k) \cdot \Delta V(k) > 0 \\ V_{ref}(k) - \Delta V_{step}, & \Delta P(k) \cdot \Delta V(k) < 0 \\ V_{ref}(k), & \Delta P(k) = 0 \end{cases} \tag{33}$$

where ΔV_{step} is the fixed perturbation step size. If the power increases after a voltage perturbation ($\Delta P(k) \cdot \Delta V(k) > 0$, the reference voltage is perturbed in the same direction; if the power decreases ($\Delta P(k) \cdot \Delta V(k) < 0$, the perturbation direction is reversed; and if the power remains unchanged ($\Delta P(k) = 0$, the algorithm holds the current reference voltage, indicating that the operating point coincides with a maximum power point. This procedure is repeated continuously, allowing the operating point to track the maximum power point under varying irradiance conditions [11,65].

To mitigate the small steady-state oscillation inherent to the fixed-step P&O rule, the Incremental Conductance (IC) algorithm evaluates the MPP condition directly, exploiting the fact that, at the maximum power point, the derivative of the array power with respect to its voltage vanishes [16,17,66]. Since $P = V \cdot I$, this condition can be expressed as

$$dP/dV = I + V \cdot (dI/dV) = 0 \qquad \rightarrow \qquad dI/dV = -I/V \tag{34}$$

where I/V represents the instantaneous conductance of the array and dI/dV represents its incremental conductance. At each sampling instant k, the algorithm computes the discrete approximations

$$\Delta I(k) = I(k) - I(k-1), \qquad \Delta V(k) = V(k) - V(k-1) \tag{35}$$

and updates the reference voltage according to

$$V_{ref} = \begin{cases} V_{ref}(k), & \Delta V(k) = 0 \; and \; \Delta I(k) = 0 \\ V_{ref}(k) + \Delta V_{step}, & \Delta V(k) = 0 \; and \; \Delta I(k) > 0 \\ V_{ref}(k) - \Delta V_{step}, & \Delta V(k) = 0 \; and \; \Delta I(k) < 0 \\ V_{ref}(k), & \Delta V(k) \neq 0 \; and \; \frac{\Delta I(k)}{\Delta V(k)} = -\frac{I(k)}{V(k)} \\ V_{ref}(k) + \Delta V_{step}, & \Delta V(k) \neq 0 \; and \; \frac{\Delta I(k)}{\Delta V(k)} > -\frac{I(k)}{V(k)} \\ V_{ref}(k) - \Delta V_{step}, & \Delta V(k) \neq 0 \; and \; \frac{\Delta I(k)}{\Delta V(k)} < -\frac{I(k)}{V(k)} \end{cases} \quad (36)$$

where ΔV_{step} is the fixed perturbation step size. The first two branches of Equation (36) handle the special case in which the voltage has not changed between consecutive samples ($\Delta V(k) = 0$, e.g., immediately after the reference voltage has settled): if the current also remains unchanged, the array is still operating at the MPP, and no action is taken; if the current changes, this indicates a variation in irradiance, and the reference voltage is adjusted in the direction consistent with the sign of $\Delta I(k)$. The remaining branches implement the incremental-conductance comparison of Equation (34) directly: when $\Delta I(k)/\Delta V(k)$ equals $-I(k)/V(k)$, the operating point coincides with the MPP and V_{ref} is held constant; when it exceeds $-I(k)/V(k)$, the operating point lies to the left of the MPP and V_{ref} is increased; and when it is smaller, the operating point lies to the right of the MPP and V_{ref} is decreased.

While Equation (36) theoretically allows the reference voltage to remain exactly constant once the MPP condition is satisfied—avoiding the continuous perturbation around the MPP characteristic of P&O—both algorithms remain vulnerable to a more fundamental limitation under partial shading conditions (PSCs): the resulting PV power–voltage (P–V) characteristic exhibits multiple local maxima, giving rise to multiple local maximum power points (LMPPs) in addition to the global maximum power point (GMPP), and each algorithm relies exclusively on local information obtained around the current operating point to decide its next step [29,67]. In the case of P&O-MPPT, Equation (33) drives the reference voltage toward whichever maximum lies in the direction of increasing power from the current operating point, without any information about the global shape of the P–V curve. Similarly, in the case of IC-MPPT, the MPP condition $dI/dV = -I/V$ in Equation (34) is satisfied at every local maximum power point, not only at the global one, so Equation (36) provides no means of distinguishing an LMPP from the GMPP. Consequently, both the P&O-MPPT and IC-MPPT algorithms may become trapped at an LMPP under partial shading, leading to reduced energy harvesting and lower overall system efficiency [13,21].

3.3. PSO-MPPT Algorithm

To overcome the tendency of the conventional MPPT algorithms to converge to a local maximum power point (LMPP) under partial shading conditions (PSCs), a Particle Swarm Optimization (PSO)-based MPPT algorithm is proposed. PSO is a population-based metaheuristic in which a swarm of candidate solutions ("particles"), each representing a candidate reference voltage V_i iteratively updates its position within the search space based on its own best-known position and the best-known position of the swarm as a whole [20,68]. Unlike the conventional P&O algorithm, which perturbs the operating point in a single direction and is therefore prone to becoming trapped at the nearest local maximum, the population-based nature of PSO enables the simultaneous evaluation of multiple candidate operating points across the search space, which in principle allows the algorithm to escape LMPPs and converge toward the GMPP under multimodal P–V characteristics.

The velocity and position of each particle i are updated at each iteration t according to [23,26]

$$v_i^{t+1} = w \cdot v_i^t + c_1 \cdot r_1 \cdot \left(p_{best,i} - x_i^t\right) + c_2 \cdot r_2 \cdot \left(g_{best} - x_i^t\right) \quad (37)$$

$$x_i^{t+1} = x_i^t + v_i^{t+1} \tag{38}$$

where x_i denotes the candidate reference voltage of the particle i, w is the inertia weight, c_1 and c_2 are the cognitive and social acceleration coefficients, r_1 and r_2 are uniformly distributed random numbers in $[0|1]$, $p_{best,i}$ is the best position found so far by the particle i, and g_{best} is the best position found so far by the entire swarm. The fitness of each candidate position is evaluated directly from the power delivered by the PV array,

$$f(V) = P_{pv}(V) = V{\cdot}I(V) \tag{39}$$

which is maximized by the swarm over successive iterations. The power is computed from the measured array voltage and current, $P_{pv} = V_{pv}{\cdot}I_{pv}$, so the PSO requires V and I sensors; the irradiances are not used in the fitness function.

A conventional PSO implementation initializes the swarm uniformly across the entire feasible voltage range $[0|V_{oc}]$, which requires a comparatively large number of particles and iterations to reliably locate the GMPP, particularly when the search space must be re-explored after every irradiance transition. To reduce this computational burden without compromising tracking accuracy, the PSO-MPPT algorithm proposed in this work exploits a structural property of the PV array under study: as shown by the offline characterization performed to generate the ANN training dataset (Section 4.1), the GMPP voltage does not vary continuously across the feasible range but instead consistently falls within a small number of well-defined voltage regions, hereafter referred to as clusters. For the PV array configuration considered in this study, three such clusters were identified empirically from the P–V curves of the 1000 scenarios at a cell temperature of 25 °C (Section 4.1), centered approximately at 20 V, 45.5 V, and 71 V, each with a characteristic half-width (2, 4.5 and 7 V, respectively) reflecting the range of GMPP voltages observed for the shading patterns that map to that cluster. A fourth candidate, at 66 V (half-width 5 V), was added to the probe to cover the case of high and uniform irradiance, whose single peak (about 65 V) lies between the 45.5 V and 71 V clusters. Because the centers and half-widths are fixed, they correspond to 25 °C; the effect of other cell temperatures, and a compensation of the ranges, are evaluated in Section 4.8.

This prior knowledge is incorporated into the swarm initialization: instead of sampling particle positions uniformly, each particle is seeded around one of the K known cluster centers c_k with probability p_k proportional to the relative frequency with which that cluster was observed as the GMPP location during the offline characterization,

$$x_i^0 = c_k + \delta_i, \qquad \delta_i \sim u(-h_k, h_k), \qquad k \sim Categorical(p_1, \ldots, p_K) \tag{40}$$

where h_k is the empirically observed half-width of the cluster k. Rather than allowing the swarm to explore the full continuous range between clusters, the algorithm first performs a directed evaluation ("probe") of the K cluster centers and of the additional candidate at 66 V (half-width 5 V), selecting the candidate that yields the highest measured power according to Equation (39); a localized PSO refinement, restricted to the neighborhood $[c_k - h_k,\ c_k + h_k]$ of the winning cluster, is subsequently executed to converge on the precise GMPP voltage within that region. This two-stage search substantially reduces both the number of power evaluations and the associated transient disturbance imposed on the DC–DC converter and the motor–pump assembly, compared with an unconstrained swarm search over the entire voltage range.

Furthermore, unlike the conventional MPPT algorithms, which perturb the reference voltage at every sampling instant, and unlike a PSO implementation that re-evaluates the swarm continuously, the proposed algorithm operates in an event-triggered manner: the reference voltage is held constant at the last converged GMPP while the irradiance levels

G_1, G_2, and G_3 remain within a defined tolerance of the values recorded at the previous convergence. A new search is triggered only once a sustained deviation

$$max\left(\left|G_j(t) - G_j^{ref}\right|\right) > \Delta G_{th}, \qquad j \in \{1,2,3,\} \tag{41}$$

is detected after the irradiance signals have remained stable for a minimum dwell time, which prevents the algorithm from initiating a search while the irradiance is still transitioning between operating conditions. This design choice minimizes unnecessary perturbation of the operating point during steady-state operation, while retaining the ability of the population-based search to recover the GMPP whenever the irradiance distribution across the array changes. In this scheme, the irradiances G_1, G_2, and G_3 are used only to detect a change in the shading pattern and trigger a new search, not to select the cluster, which is chosen from the measured power during the probe.

The cluster centers and half-widths were obtained from P–V curves at a cell temperature of 25 °C; the effect of other cell temperatures on the fixed ranges and compensation is evaluated in Section 4.8.

3.4. ANN-MPPT Algorithm

To overcome the limitations of the conventional MPPT algorithms under partial shading conditions, an Artificial Neural Network (ANN)-based MPPT algorithm is implemented. Unlike conventional search-based methods, the ANN is trained to directly estimate the optimal reference voltage corresponding to the global maximum power point (GMPP) from the irradiance conditions of the PV array. Consequently, the proposed approach has the potential to avoid convergence to local maximum power points (LMPPs) and improve the tracking performance under complex shading scenarios [29,64].

The proposed ANN uses only the three measured irradiance levels (G_1, G_2, and G_3), from which additional input features are computed, as illustrated in Figure 11. The network is trained on P–V curves at a cell temperature of 25 °C; the effect of other cell temperatures is evaluated in Section 4.8.

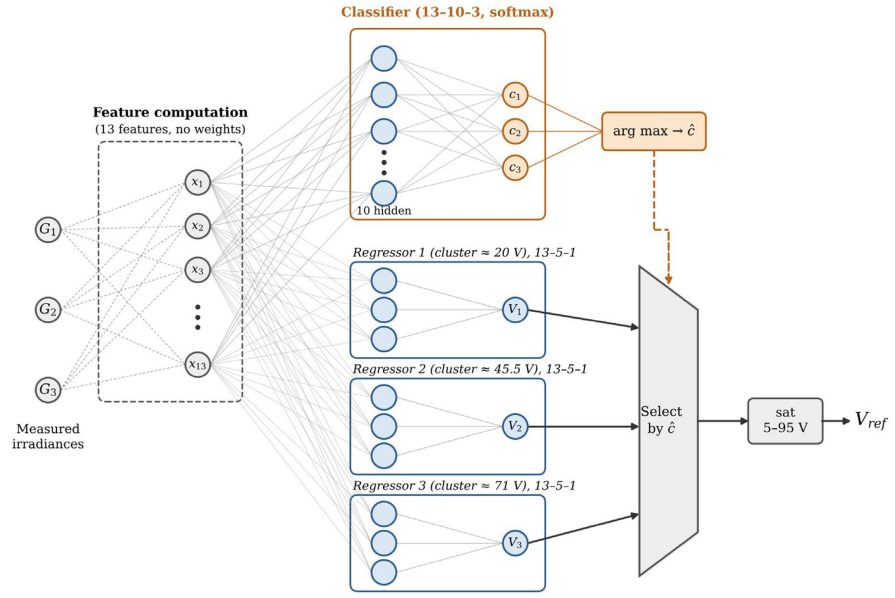


Figure 11. Architecture of the proposed ANN-MPPT algorithm. The 13 features computed from the measured irradiances G_1, G_2 and G_3 (dashed box, no trainable weights) feed a classifier that selects the GMPP voltage cluster and three cluster-specific regressors; the classifier output ĉ (dashed arrow) selects the regressor whose estimate, limited to 5–95 V, is the reference voltage V_{ref}. Vertical dots indicate neurons that are not drawn; for clarity, not all neurons are drawn.

The GMPP voltage does not vary smoothly with the irradiance: as the shading pattern changes, the GMPP jumps between the three voltage clusters identified in Section 4.1. For this reason, the ANN-MPPT algorithm uses two stages: a classifier that selects the cluster and a set of regressors, one per cluster, that estimate the voltage within it. Previous ANN-based MPPT controllers, including those for PV pumping, generally use a single feedforward network that maps the irradiance, or the voltage and current, to the reference voltage [28,62,67], or combine it with a perturbative search [39]; the same holds for ANN-assisted GMPP tracking under partial shading [37,38,69]. Among the studies we reviewed, we did not find one that first classifies the voltage cluster of the GMPP and then applies a regressor specific to that cluster; in our case, this separation was adopted because a single network gave large estimation errors in some scenarios, as shown below.

$$x = \left[G_1,\ G_2,\ G_3,\ G_1/G_{max},\ G_2/G_{max},\ G_3/G_{max},\ G_{(1)},\ G_{(2)},\ G_{(3)},\ G_2 - G_1,\ G_3 - G_2,\ G_{min},\ G_{max} - G_{min}\right]^T \quad (42)$$

where G_{max} and G_{min} are the largest and smallest of the three irradiances, and $G_{(1)} \leq G_{(2)} \leq G_{(3)}$ are the irradiances sorted in ascending order. In the first stage, a feedforward classifier with 13 inputs, one hidden layer of ten neurons and three outputs estimates the cluster of the GMPP voltage:

$$\hat{c} = \text{argmax}_k \left(\text{softmax}(W_2 \tanh(W_1 x + b_1) + b_2)_k\right) \quad (43)$$

where x is the input feature vector of Equation (42); W_1 and b_1 are the weights and biases of the hidden layer, whose activation function is $\tanh(\cdot)$; W_2 and b_2 are the weights and biases of the output layer; $\text{softmax}(\cdot)$ converts the three output values into probabilities for each cluster; argmax_k selects the index of the cluster with the highest probability; and $\hat{c}$ is the cluster predicted by the network.

In the second stage, a regression network selected by $\hat{c}$, with 13 inputs, one hidden layer of five neurons and one output, estimates the reference voltage:

$$V_{ref} = \text{sat}\left(W_2^{(\hat{c})} \tanh\left(W_1^{(\hat{c})} x + b_1^{(\hat{c})}\right) + b_2^{(\hat{c})}\right) \quad (44)$$

where $W_1^{(\hat{c})}$, $b_1^{(\hat{c})}$, $W_2^{(\hat{c})}$ and $b_2^{(\hat{c})}$ are the weights and biases of the hidden and output layers of the regressor trained for the predicted cluster $\hat{c}$, with a $\tanh(\cdot)$ activation in the hidden layer and a linear output, and $\text{sat}(\cdot)$ limits V_{ref} to the range 5–95 V. The three clusters correspond to GMPP voltages of about 20, 45.5 and 71 V, and the cluster labels were assigned with limits at 32 V and 58 V. Since the features are computed from G_1, G_2 and G_3, the sensing requirement is the same as for a network that uses the three irradiances directly.

The classifier was trained with the scaled conjugate gradient algorithm and the cross-entropy loss, and each regressor with the Levenberg–Marquardt algorithm and the mean squared error, using only the training scenarios of its cluster. The 1000 scenarios of Section 4.1 were divided at the scenario level into 700 for training, 150 for validation and 150 for testing, with a fixed random seed. Each scenario belongs to only one subset; however, because the irradiances were drawn from a discrete set, the same irradiance combination may occur in the training and the test subsets. On the 150 test scenarios, the classifier selected the correct cluster in all cases, and the power obtained at the estimated voltage was on average 99.99% of the GMPP power (minimum 99.96%). For comparison, a single 3–10–1 regression network trained on the same irradiance triplet reached a mean of 93.9% of the GMPP power, with an estimation error above 12 V in 16 of the 150 test scenarios; increasing its hidden layer to 20 or 30 neurons did not improve the result, which indicates that the limitation lies in the structure of the mapping and not in the network size. This was the reason for adopting the two-stage structure. The comparison among variants was carried out on the same test scenarios, so these figures should be read as indicative of the behavior on shading patterns drawn from the same distribution as the training data.

4. Results

4.1. PV Array Dataset Generation

To generate the training dataset for the proposed ANN-MPPT algorithm, and to identify cluster centers for the PSO-MPPT algorithm, the load was disconnected from the PV array and replaced with a controlled voltage source. A voltage-sweep algorithm was implemented to obtain the current–voltage (I–V) and power–voltage (P–V) characteristic curves of the PV array under randomly varied irradiance conditions, thereby emulating a wide range of partial shading patterns. A total of 1000 irradiance scenarios were generated by drawing the irradiance levels of each PV group (G_1, G_2, and G_3) independently and at random from the discrete set {200, 300, ..., 1000} W/m^2 (steps of 100 W/m^2), using a fixed random seed. For each scenario, the resulting P–V curve was analyzed to identify the global maximum power point (GMPP) and its corresponding voltage V_{mpp}. Figure 12 shows the superimposed P–V curves obtained for the 1000 simulated scenarios, together with the identified GMPP for each case. As expected, non-uniform irradiance distributions produce P–V curves with multiple local maxima, whereas uniform or near-uniform conditions yield a single, well-defined peak. The resulting dataset, composed of the triplet (G_1, G_2, G_3) as inputs and the corresponding Vmpp as output, was subsequently used to train the ANN-MPPT described in Section 3.4.

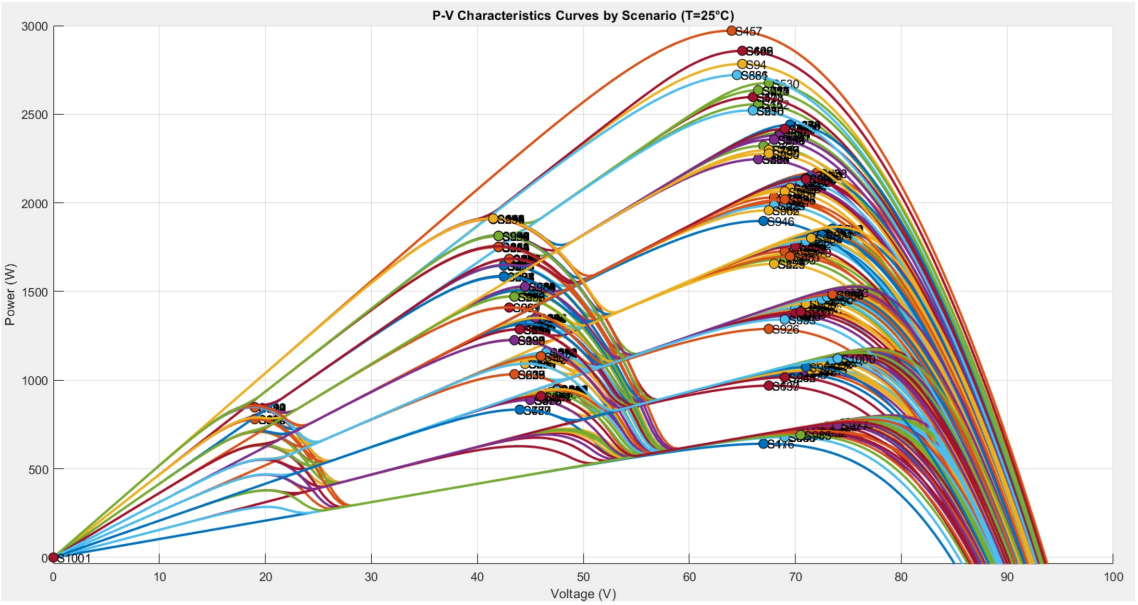


Figure 12. P–V characteristic curves obtained for 1000 randomly generated partial shading scenarios at a cell temperature of 25 °C, showing the identified global maximum power point (GMPP) for each case. This dataset was used to train the proposed ANN-based MPPT algorithm. Each curve is one scenario and each marker its GMPP; colors are only used to distinguish the curves. This dataset was used to train the proposed ANN-MPPT algorithm.

4.2. Identification of GMPP and LMPP Under Representative Shading Scenarios

To evaluate the tracking performance of the three MPPT strategies under controlled and reproducible conditions, five representative irradiance scenarios were selected (Table 3), ranging from uniform irradiance to severe partial shading with pronounced power mismatches between PV groups.

Table 3. Selected irradiance scenarios for MPPT performance evaluation.

Scenario	G1 (W/m^2)	G2 (W/m^2)	G3 (W/m^2)
S1	500	500	500
S2	800	900	300
S3	700	800	200
S4	700	800	500
S5	800	800	300

The P–V characteristic curves obtained for each scenario are shown in Figure 13. Under uniform irradiance (S1), the PV array reaches its maximum power point at approximately 67.25 V, delivering 1596.35 W. In contrast, scenarios S2, S3, and S5, characterized by larger irradiance mismatches between PV groups, present two distinct power peaks: a local maximum power point (LMPP) located at higher voltage around 76.25–77.25 V and a global maximum power point (GMPP) located at lower voltage around 42.25–43.25 V, with the GMPP delivering substantially more power than the LMPP—for instance, in scenario S3, the GMPP (1464.17 W) nearly doubled the power available at the LMPP (784.42 W), corresponding to a 86.66% increase. Scenario S4, with a smaller irradiance mismatch, also shows two peaks but with a narrower power gap between them.

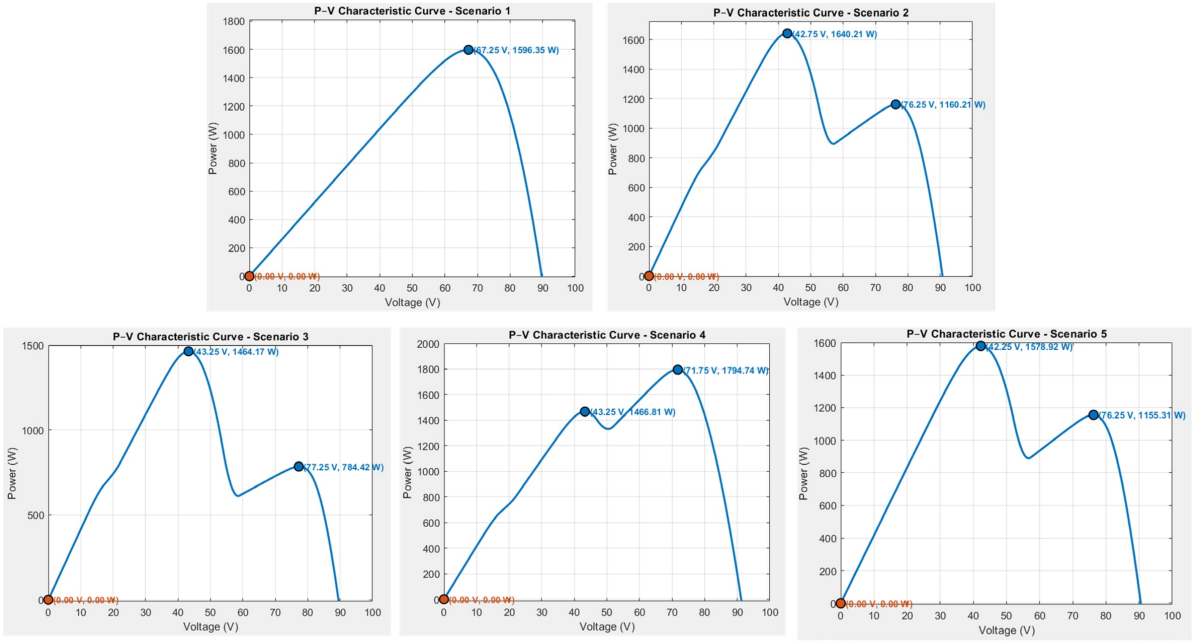


Figure 13. P–V characteristic curves of the PV array for the five selected irradiance scenarios (S1–S5), illustrating the presence of a single maximum power point under uniform irradiance (S1) and multiple local maxima (LMPP) alongside the global maximum power point (GMPP) under partial shading conditions (S2, S3, S4, S5).

These results confirm that partial shading conditions consistently generate multimodal P–V characteristics in the proposed PV array configuration, making these scenarios suitable benchmarks for assessing the risk of LMPP convergence under each MPPT strategy.

4.3. Performance of IC-MPPT Algorithm

The five irradiance scenarios (Table 3) were applied sequentially (four-second intervals) to the PVSWPS model under the conventional IC-MPPT algorithm [16,17,19]. Figure 14 presents the resulting irradiance profile, PV array and motor voltages/currents/power, pump flow rate, and cumulative pumped volume.

During scenario S1 (uniform irradiance), IC-MPPT converges to the single GMPP (1596.35 W at 67.25 V, a tracking error of only 0.63%), though the PV array voltage exhibits continuous small-amplitude perturbation consistent with the fixed-step decision rule of Equation (36), since the equality condition $\Delta I(k)/\Delta V(k) = -I(k)/V(k)$ is rarely satisfied exactly due to measurement noise and the discrete resolution of ΔV_{step}. In scenarios S2, S3, and S5, however, the algorithm converges to the LMPP (76.25–77.25 V) instead of the GMPP (42.25–43.25 V), producing the largest tracking error in this scenario set—45.97% in S3. Only in S4, with a smaller irradiance mismatch, does the algorithm approach the GMPP more closely (error: 0.84%).

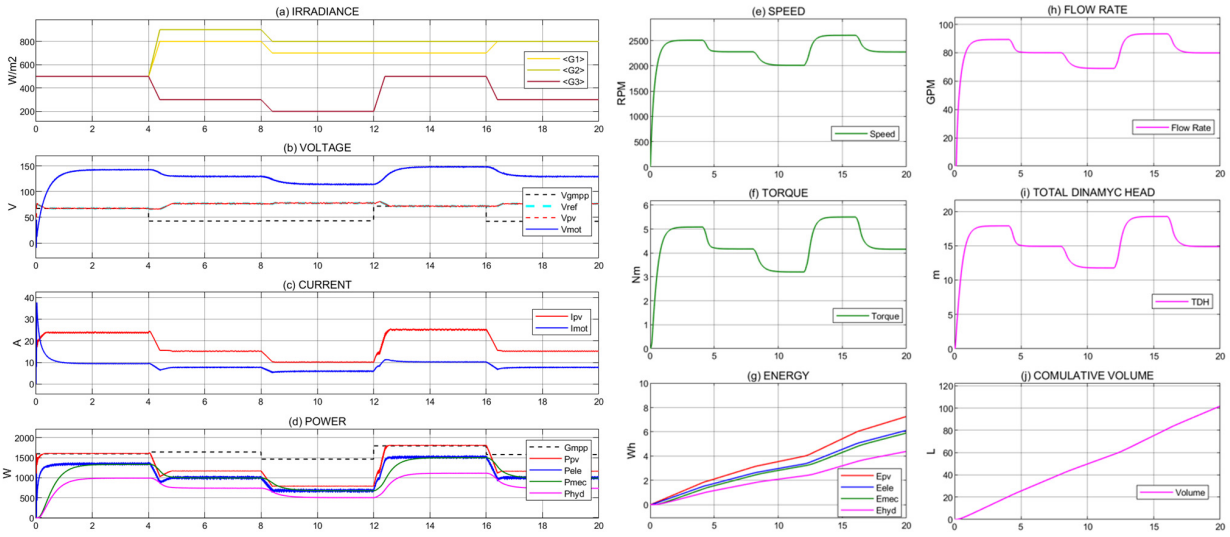


Figure 14. Dynamic response of the PVSWPS under the conventional IC-MPPT algorithm [16,17,19] across the five irradiance scenarios: (**a**) irradiance profile; (**b**) PV array and motor voltage; (**c**) PV array and motor current; (**d**) power; (**e**) motor speed; (**f**) motor torque; (**g**) energy; (**h**) pump flow rate; (**i**) pump total dynamic head; and (**j**) cumulative pumped volume. LMPP convergence is observed in S2, S3, and S5.

This LMPP entrapment reduces pump flow rate during S2, S3, and S5 to approximately 65–80 gpm, and limits the cumulative pumped volume to 101.9 L over the 20 s simulation period. Table 4 summarizes the per-scenario tracking error and cumulative energy/volume performance.

Table 4 also reports the energy at each stage of the system: E_{pv} at the PV array terminals, E_{ele} at the motor terminals (converter output), E_{mec} at the motor shaft and E_{hyd} at the pump hydraulic output. The stage efficiencies are $\eta_{conv} = E_{ele}/E_{pv}$, $\eta_{motor} = E_{mec}/E_{ele}$, $\eta_{pump} = E_{hyd}/E_{mec}$ and the overall efficiency is $\eta_{tot} = E_{hyd}/E_{pv}$. Under IC-MPPT they are 84.25%, 96.45%, 74.33% and 60.4%, respectively. Notably, the converter efficiency is the highest of the three algorithms although IC-MPPT delivers the lowest volume: the higher LMPP voltage (76.25–77.25 V) demands substantially less current than the GMPP voltage (42.25–43.25 V) at equivalent power, which is consistent with lower conduction losses in the converter. In other words, LMPP entrapment moves the converter closer to its most efficient operating region, at the cost of extracting far less power from the PV array ($E_{pv} = 7.257$ Wh), a trade-off examined further in Section 4.6.

Table 4. Steady-state power tracking, energy performance, and pumped water volume for the IC-MPPT algorithm [16,17,19] across the evaluated scenarios.

Scenario	GMPP kW	Ppv kW	Error %	E_{pv} Wh	E_{ele} Wh	E_{mec} Wh	E_{hyd} Wh	η_{conv} %	η_{motor} %	η_{pump} %	η_{tot} %	Cum. Vol. L
S1	1.596	1.606	0.63	-	-	-	-	-	-	-	-	-
S2	1.640	1.170	28.65	-	-	-	-	-	-	-	-	-
S3	1.464	0.791	45.97	-	-	-	-	-	-	-	-	-
S4	1.794	1.809	0.84	-	-	-	-	-	-	-	-	-
S5	1.578	1.165	26.17	-	-	-	-	-	-	-	-	-
Cumulative	-	-	-	7.257	6.114	5.897	4.383	84.25	96.45	74.33	60.4	101.9

To check whether the limitation of IC-MPPT is specific to the fixed step, an improved version with a dead-band (2% of the conductance I/V) and an adaptive step (proportional to |dP/dV|, limited to 0.1–3 V) was simulated under the same five scenarios. The improved version reduces the voltage ripple (standard deviation of about 0.21–0.26 V against 0.41–0.49 V) and settles within ±2% in 0.16–0.52 s instead of 3.5–3.9 s, but it still remains at the LMPP in S2, S3 and S5, with tracking errors of 28.7%, 46.0% and 26.2%, and the same cumulative volume (101.9 L). These variants refine the local search but do not solve the global-search problem.

4.4. Performance of PSO-MPPT Algorithm

The same five-scenario sequence (Table 3) was applied to the PVSWPS model under the proposed PSO-based MPPT algorithm [20,23,26]; results are shown in Figure 15.

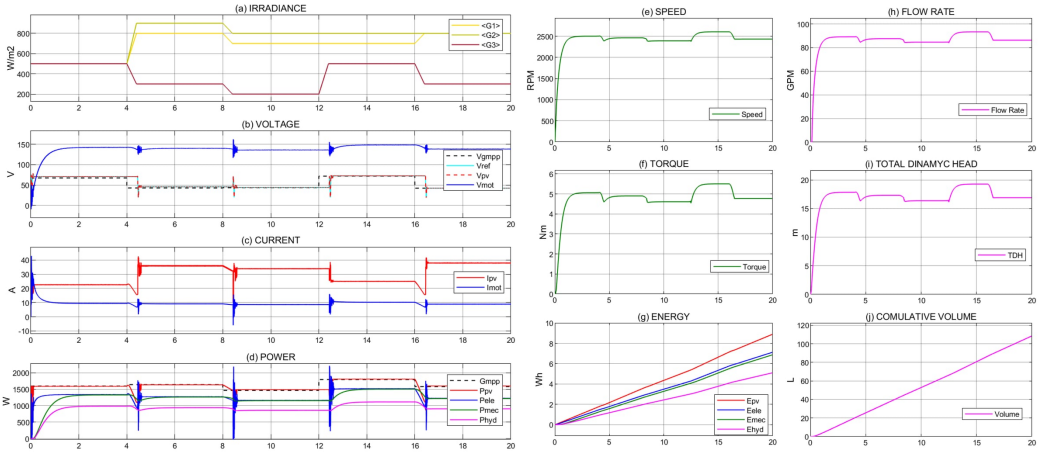


Figure 15. Dynamic response of the PVSWPS under the PSO-MPPT algorithm [20,23,26] across the five irradiance scenarios: (**a**) irradiance profile; (**b**) PV array and motor voltage; (**c**) PV array and motor current; (**d**) power; (**e**) motor speed; (**f**) motor torque; (**g**) energy; (**h**) pump flow rate; (**i**) pump total dynamic head; and (**j**) cumulative pumped volume.

During S1 (uniform irradiance), the swarm—initialized around the empirically known cluster centers (Sections 3.3 and 4.1)—converges to the single MPP without an extensive search. Following each irradiance transition (S1→S2, S2→S3, S3→S4, S4→S5), a brief transient disturbance appears in V_{pv}, I_{pv}, and P_{pv}, corresponding to the directed probe of candidate GMPP clusters and subsequent localized refinement; these disturbances are visibly shorter and more contained than an exhaustive, unconstrained search would produce, since the search is restricted to the neighborhood of the known voltage clusters. The PV array voltage then settles at the correct GMPP for each scenario, including S2, S3, and S5, where IC-MPPT became trapped at the LMPP (Section 4.3).

This consistent tracking yields a markedly lower error across all five scenarios (0.2–1.33%, Table 5)—substantially below IC-MPPT's 26–46% in the same scenarios—keeping pump flow rate at approximately 85–93 gpm throughout, without the reductions seen under IC-MPPT. PSO-MPPT delivered a cumulative pumped volume of 108.5 L over the 20 s simulation window, an increase of approximately 6.5% relative to IC-MPPT's 101.9 L, and its hydraulic energy is 16.4% higher (5.102 versus 4.383 Wh). The converter efficiency is 80.11%, lower than IC-MPPT's 84.25%, while the motor (96.46%) and pump (74.28%) efficiencies are practically unchanged (η_{tot} = 57.40%); this trade-off is examined in Section 4.6. Table 5 summarizes the per-scenario tracking error and the cumulative energy and volume performance of the PSO-MPPT algorithm.

Table 5. Steady-state power tracking, energy performance, and pumped water volume for the PSO-MPPT algorithm [20,23,26] across the evaluated scenarios.

Scenario	GMPP kW	Ppv kW	Error %	E_{pv} Wh	E_{ele} Wh	E_{mec} Wh	E_{hyd} Wh	η_{conv} %	η_{motor} %	η_{pump} %	η_{tot} %	Cum. Vol. L
S1	1.596	1.604	0.50	-	-	-	-	-	-	-	-	-
S2	1.640	1.649	0.55	-	-	-	-	-	-	-	-	-
S3	1.464	1.467	0.20	-	-	-	-	-	-	-	-	-
S4	1.794	1.806	0.67	-	-	-	-	-	-	-	-	-
S5	1.578	1.599	1.33				-	-	-	-	-	-
Cumulative	-	-	-	8.889	7.121	6.869	5.102	80.11	96.46	74.28	57.40	108.5

4.5. Performance of ANN-MPPT Algorithm

The same five-scenario sequence was applied with the PVSWPS operating under the proposed ANN-based MPPT algorithm [27–30]; results are shown in Figure 16.

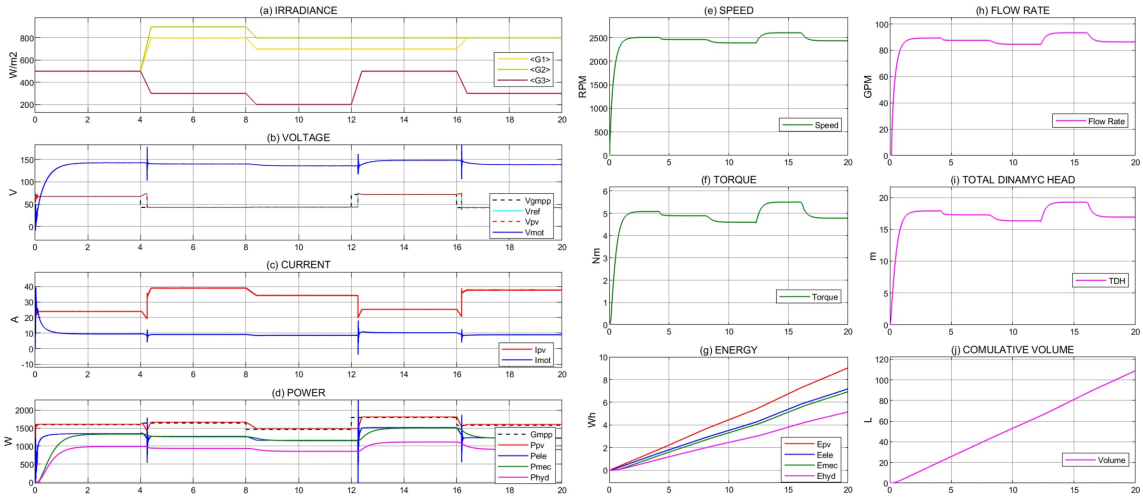


Figure 16. Dynamic response of the PVSWPS under the ANN-MPPT algorithm [27–30] across the five irradiance scenarios: (**a**) irradiance profile; (**b**) PV array and motor voltage; (**c**) PV array and motor current; (**d**) power; (**e**) motor speed; (**f**) motor torque; (**g**) energy; (**h**) pump flow rate; (**i**) pump total dynamic head; and (**j**) cumulative pumped volume.

Unlike IC-MPPT, ANN-MPPT converges to the GMPP in all five scenarios, including S2, S3, and S5, where IC-MPPT became trapped at the LMPP (Section 4.3). V_{pv} shifts directly toward the GMPP voltage for each new irradiance condition, with only brief transients corresponding to the PI controller's settling time, and without the oscillatory search behavior of the IC-MPPT decision rule. Tracking error remains consistently low across all five scenarios (0.63–1.46%, Table 6)—comparable to PSO-MPPT (0.2–1.33%, Section 4.4) and

substantially lower than IC-MPPT's 26–46% in the same shading scenarios. Consequently, pump flow rate stays at approximately 85–93 gpm across all scenarios, and the cumulative pumped volume reaches 109.0 L, an increase of approximately 7.0% relative to the 101.9 L obtained with IC-MPPT (hydraulic energy +17.5%). The converter efficiency is 79.52%, the lowest of the three, with motor 96.49%, pump 74.26% and $\eta_{tot} = 56.99\%$.

Table 6 summarizes the per-scenario tracking error and the cumulative energy and volume performance of the ANN-MPPT algorithm.

Table 6. Steady-state power tracking, energy performance, and pumped water volume for the ANN-MPPT algorithm [27–30] across the evaluated scenarios.

Scenario	GMPP kW	Ppv kW	Error %	E_{pv} Wh	E_{ele} Wh	E_{mec} Wh	E_{hyd} Wh	η_{conv} %	η_{motor} %	η_{pump} %	η_{tot} %	Cum. Vol. L
S1	1.596	1.606	0.63	-	-	-	-	-	-	-	-	-
S2	1.640	1.664	1.46	-	-	-	-	-	-	-	-	-
S3	1.464	1.484	1.37	-	-	-	-	-	-	-	-	-
S4	1.794	1.808	0.78	-	-	-	-	-	-	-	-	-
S5	1.578	1.601	1.46	-	-	-	-	-	-	-	-	-
Cumulative	-	-	-	9.039	7.188	6.936	5.151	79.52	96.49	74.26	56.99	109.0

4.6. Comparative Summary

Table 7 summarizes the operating regime (GMPP or LMPP) reached by each MPPT strategy in each of the five evaluated scenarios.

Table 7. Operating point reached by each MPPT algorithm under the evaluated shading scenarios.

Scenario	IC-MPPT	PSO-MPPT	ANN-MPPT
S1	GMPP	GMPP	GMPP
S2	LMPP	GMPP	GMPP
S3	LMPP	GMPP	GMPP
S4	GMPP	GMPP	GMPP
S5	LMPP	GMPP	GMPP

These results confirm that, while all three algorithms perform similarly under uniform or mildly mismatched irradiance conditions (S1 and S4), the conventional IC-MPPT algorithm is highly susceptible to LMPP convergence under pronounced partial shading (S2, S3, and S5). In contrast, both intelligent strategies consistently identify the GMPP regardless of the shading pattern. Table 8 consolidates the quantitative tracking, energy, and volume metrics for the three algorithms, previously presented individually in Tables 4–6.

As shown in Table 8, the mean tracking error under IC-MPPT (20.45%) is more than an order of magnitude higher than under PSO-MPPT (0.65%) or ANN-MPPT (1.14%), directly reflecting the three scenarios (S2, S3, S5) in which the conventional algorithm became trapped at the LMPP. This improved tracking accuracy translates into a modest but consistent gain in pumped water volume: PSO-MPPT and ANN-MPPT deliver 108.5 L and 109.0 L, respectively, over the 20 s simulation window, corresponding to increases of approximately 6.5% and 7.0% relative to the 101.9 L obtained with IC-MPPT. The difference between the two intelligent strategies is small (about 0.5% in volume): PSO-MPPT shows the lower mean tracking error, whereas ANN-MPPT delivers slightly more water. Given the stochastic nature of the PSO search, this difference should not be read as a ranking, and the results indicate that both approaches—one based on a directed population search, the other on a pre-trained nonlinear mapping—achieve similar practical outcomes once the GMPP entrapment problem is resolved.

Table 8. Quantitative comparison of tracking accuracy, energy performance, and pumped water volume across the three evaluated MPPT algorithms.

Metric	IC-MPPT	PSO-MPPT	ANN-MPPT
Required sensors	V, I	V, I, G1, G2, G3	G1, G2, G3
Scenarios tracking GMPP	2/5	5/5	5/5
Tracking error range (%)	0.63–45.97	0.2–1.33	0.63–1.46
Mean tracking error (%)	20.45	0.65	1.14
Converter efficiency, η_{conv} (%)	84.25	80.11	79.52
Motor efficiency, η_{motor} (%)	96.45	96.46	96.49
Pump efficiency, η_{pump} (%)	74.33	74.28	74.26
Overall efficiency, η_{tot} (%)	60.4	57.40	56.99
Hydraulic energy, E_{hyd} (Wh)	4.383	5.102	5.151
Cumulative pumped volume (L)	101.9	108.5	109.0
Volume increase vs. IC-MPPT (%)	-	6.5	7.0

Figure 17 overlays the three strategies over the five scenarios. In S2, S3 and S5, IC-MPPT stays near the LMPP voltage (about 77 V), so the array power remains at 1.17, 0.79 and 1.16 kW against GMPP values of 1.64, 1.46 and 1.58 kW, and the pump flow falls to about 80, 69 and 80 gpm. PSO-MPPT and ANN-MPPT move to the GMPP voltage after each irradiance step and keep the flow at about 85–93 gpm. After each irradiance step, the pump flow settled within ±2% of its final value in less than 1.5 s for the three algorithms. The array voltage settled within the same band in 0.1–0.6 s with PSO-MPPT and ANN-MPPT, whereas IC-MPPT, whose fixed step moves the voltage gradually, required 3.5–3.9 s. The figure also shows a difference that Tables 5 and 6 do not capture: after each step PSO-MPPT briefly visits its candidate voltages, with short drops in power and flow, whereas ANN-MPPT reaches the GMPP voltage directly from the irradiance measurements.

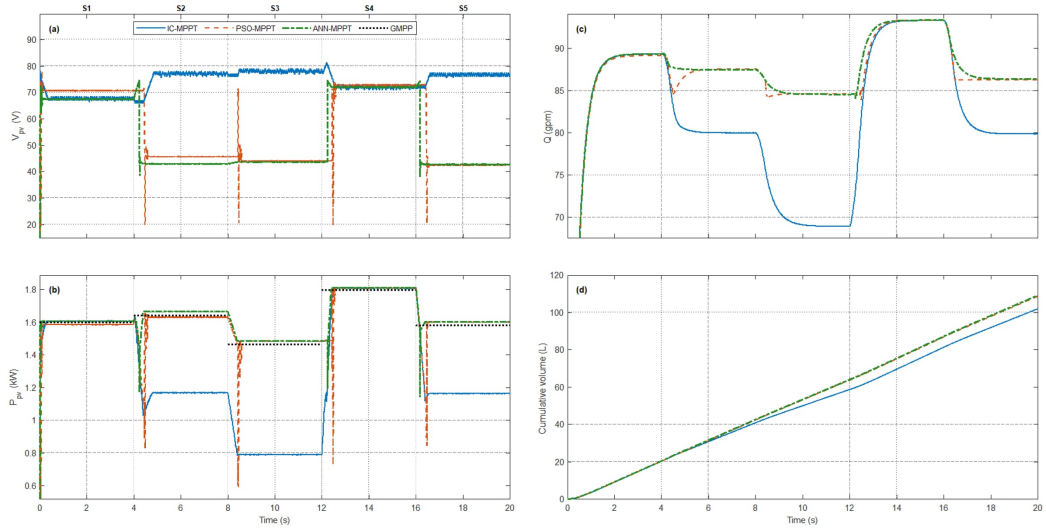


Figure 17. Comparison of IC-MPPT, PSO-MPPT and ANN-MPPT over the five evaluated scenarios: (**a**) PV array voltage, (**b**) PV array power with the GMPP of each scenario, (**c**) pump flow rate, and (**d**) cumulative pumped volume.

Computed over the last 2 s of each scenario, after the flow transient has settled, the mean flow is 82.3 gpm for IC-MPPT and 88.2 gpm for both PSO-MPPT and ANN-MPPT, a gain of 7.2%, consistent with the 6.5% and 7.0% obtained from the cumulative volume.

Notably, this gain in delivered volume comes with a lower converter efficiency: η_{conv} decreases from 84.25% (IC-MPPT) to 80.11% (PSO-MPPT) and 79.52% (ANN-MPPT), whereas η_{motor} (about 96.5%) and η_{pump} (about 74.3%) are practically identical for the three

algorithms. The lower overall efficiency therefore arises in the converter stage, which is consistent with the higher current drawn at the lower GMPP voltage; the individual loss mechanisms inside the converter were not separated. The constant pump efficiency is expected from the affinity-law model of the pump, which keeps efficiency constant with speed, and should not be read as a property of a physical pump, whose efficiency depends on its operating point.

It is also worth considering the sensing requirements of each algorithm, as this directly impacts implementation cost and system complexity. IC-MPPT relies exclusively on voltage and current measurements (V, I) at the PV array terminals, requiring no irradiance sensing. PSO-MPPT, in contrast, requires the largest sensor set among the three algorithms: V and I to evaluate the fitness function during the probe and refinement stages (Section 3.3), together with G_1, G_2, and G_3 to detect irradiance changes and trigger a new search event. ANN-MPPT requires only the three irradiance sensors (G_1, G_2, G_3) as inputs to the trained network, since the reference voltage is estimated directly without an iterative power-based search. Consequently, ANN-MPPT achieves GMPP-tracking performance comparable to PSO-MPPT (Table 8) while requiring fewer sensors than PSO-MPPT—an advantage for cost-sensitive rural deployments, provided the irradiance-to-GMPP mapping used to train the network remains valid for the specific PV array configuration and shading patterns encountered in the field.

Finally, it should be noted that, because PSO-MPPT relies on a stochastic search procedure, its cumulative volume and tracking error may exhibit some run-to-run variability across repeated simulations under identical irradiance conditions—an inherent characteristic of population-based metaheuristics not shared by the deterministic IC-MPPT and ANN-MPPT algorithms. A systematic characterization of this variability across multiple independent runs is left for future work.

4.7. Continuous Irradiance Profile

To check that the comparison does not depend on the five stepped scenarios, the three algorithms were also simulated over 60 s with a continuous irradiance profile (Figure 18a). The profile starts under clear sky (900 W/m^2 in the three groups), includes a cloud that shades G_3, G_2 and G_1 in sequence with 2 s ramps (8–34 s), a segment with rapid changes between groups (39–44.5 s), and ends with persistent partial shading (700, 800 and 200 W/m^2). The model and the algorithms are those of the previous sections.

The cumulative pumped volume was 330.5 L for IC-MPPT, 343.5 L for PSO-MPPT and 345.5 L for ANN-MPPT, i.e., gains of 3.9% and 4.6% (4.2% and 4.8% when the first 3 s are discarded) (Table 9, Figure 18c). These gains are lower than those of the five-scenario sequence because most of the profile is close to uniform irradiance, where the three algorithms coincide (106.4 gpm under clear sky). The difference appears under partial shading: IC-MPPT remains at the local maximum when G_3 is shaded (80.1 gpm against 88.9 gpm) and under persistent shading (68.9 gpm against 84.5–84.7 gpm), where the volume gain over 48–60 s reaches 17–18%. During the rapid changes, ANN-MPPT follows the irradiance slightly better than PSO-MPPT (96.8 gpm against 95.4 gpm), which needs a new search after each change. The gains therefore depend on the fraction of time under partial shading, and they are valid for the evaluated conditions.

Table 9. Pumped flow and volume over the 60 s continuous irradiance profile.

Metric	IC-MPPT	PSO-MPPT	ANN-MPPT
Cumulative pumped volume (L)	330.5	343.5	345.5
Volume increase vs. IC-MPPT (%)	-	3.9	4.6
Mean flow, whole run (gpm)	87.3	90.7	91.3
Mean flow, G_3 shaded, 13–16 s (gpm)	80.1	88.9	88.9
Mean flow, rapid changes, 39–44.5 s (gpm)	94.8	95.4	96.8
Mean flow, persistent shading, 55–60 s (gpm)	68.9	84.7	84.5

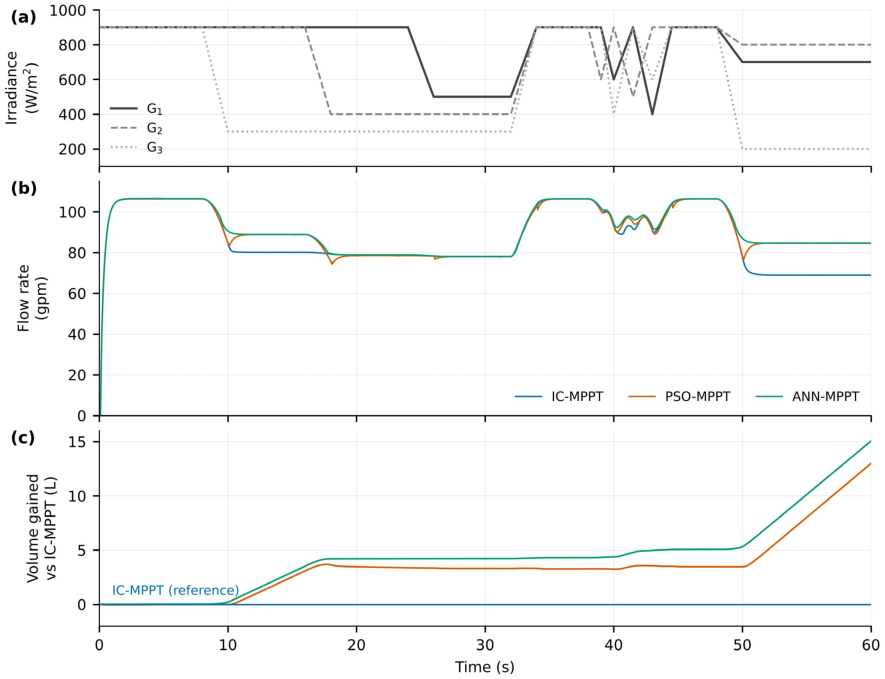


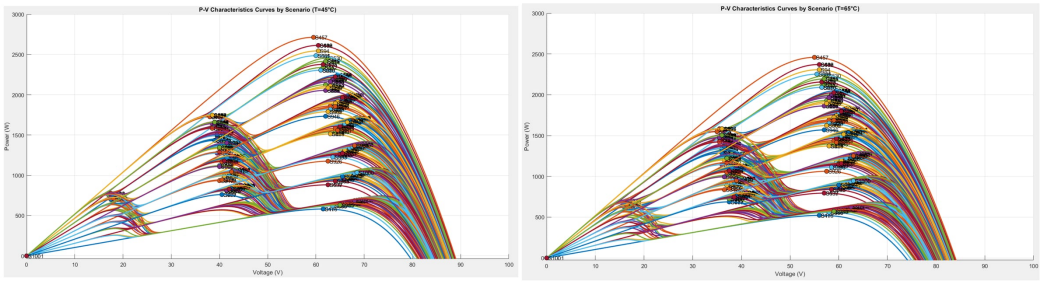
Figure 18. Continuous irradiance profile of 60 s: (**a**) irradiance of the three groups, (**b**) pump flow rate, and (**c**) volume gained with respect to IC-MPPT.

4.8. Sensitivity to Cell Temperature

The results above correspond to a cell temperature of 25 °C. Because cells in operation are typically 20–30 °C above ambient under high insolation, we evaluated the sensitivity of both algorithms to cell temperature offline, on the P–V curves of the 1000 irradiance scenarios obtained at 25, 45 and 65 °C. When the temperature rises, the GMPP voltage falls by 3.2 V on average at 45 °C and 7.5 V at 65 °C (mean coefficients of −0.17 and −0.27%/°C), and the three voltage clusters move below the fixed ranges of PSO-MPPT (Figure 12 for 25 °C, Figure 19 for 45 and 65 °C, and Table 10). The GMPP lies inside the range chosen by PSO-MPPT in 99% of the scenarios at 25 °C, 71% at 45 °C and 3% at 65 °C.

Table 10. Power obtained at the voltage selected by each algorithm, as a percentage of the GMPP power (mean/minimum over 1000 scenarios), for different cell temperatures, without and with compensation ($\beta = -0.22\%/°C$)

T (°C)	ΔV_GMPP (V)	ANN	ANN Comp.	PSO	PSO Comp.	GMPP in PSO Range (Without/with Comp.)
25	0	99.99/99.90	99.99/99.90	99.99/99.07	99.99/99.07	99%/99%
45	−3.2	93.6/84.7	99.0/97.3	99.6/88.2	99.97/95.9	71%/91%
65	−7.5	73.7/33.9	95.9/90.0	93.2/83.2	99.8/91.0	3%/75%



(**a**) (**b**)

Figure 19. P–V curves of the 1000 irradiance scenarios at a cell temperature of (**a**) 45 °C and (**b**) 65 °C, with the GMPP of each scenario marked. Each curve is one scenario; colors are only used to distinguish the curves. The curves at 25 °C are shown in Figure 12. As the temperature rises, the open-circuit voltage and the GMPP voltage decrease and the three voltage clusters move to lower voltages.

The ANN-MPPT, trained at 25 °C and without a temperature input, is the most affected: the power obtained at its reference voltage falls from 99.99% of the GMPP power at 25 °C to 93.6% at 45 °C and 73.7% at 65 °C, with a minimum of 33.9% in the worst scenario. PSO-MPPT is more robust because it measures power at its three candidates before searching around the best one (this analysis was made with the three original candidates), but it also degrades to 99.6% and 93.2%. Both degradations are explained by the mismatch between the voltages learned or assumed at 25 °C and those of the heated array.

A simple compensation, which requires only a module-temperature measurement, was then tested: the reference voltage of the ANN and the centres and ranges of PSO are multiplied by $1 + \beta(T - 25\ °\mathrm{C})$ with a single $\beta = -0.22\%/°\mathrm{C}$. With it, the ANN-MPPT reaches 99.0% at 45 °C and 95.9% at 65 °C, and PSO-MPPT 99.97% and 99.8%. The remaining loss arises because the shift is neither identical in the three clusters nor exactly linear in temperature. These results come from static P–V curves, with PSO represented by the best point inside the cluster it selects, so they indicate the size of the effect and do not replace a dynamic simulation.

5. Discussion

The results presented in Section 4 confirm that partial shading conditions (PSC) consistently generate multimodal P–V characteristics in the proposed PV array configuration, and that this multimodality directly compromises the performance of the conventional IC-MPPT algorithm. In three of the five evaluated scenarios (S2, S3, and S5), the IC-MPPT algorithm converged to the LMPP rather than the GMPP, which reduced the pump flow rate and, ultimately, the cumulative pumped volume. IC-MPPT delivered 101.9 L, compared with 108.5 L for PSO-MPPT and 109.0 L for ANN-MPPT, increases of approximately 6.5% and 7.0%, respectively. These findings are consistent with previous reports indicating that local search-based MPPT techniques are inherently vulnerable to entrapment at local maxima under non-uniform irradiance, since neither P&O nor IC can distinguish between a local and a global maximum without external information about the irradiance distribution across the array [20–22].

The proposed PSO-based and ANN-based algorithms addressed this limitation through two structurally different mechanisms. PSO-MPPT restricts its search to empirically identified voltage clusters and triggers a new search only upon a detected irradiance change, achieving consistent GMPP tracking (mean tracking error 0.65%, Table 8) at the cost of requiring the largest sensor set among the three algorithms (V, I, G_1, G_2, G_3). ANN-MPPT, in contrast, directly estimates the reference voltage from the irradiance levels of the three PV groups alone, bypassing the iterative search process altogether and achieving comparable

tracking accuracy (mean tracking error 1.14%) with the fewest sensors required (only G_1, G_2, G_3). However, this reduced sensing requirement comes with a distinct implementation trade-off: unlike PSO-MPPT, which operates directly on the live power measurements of the PV array without any prior training phase, ANN-MPPT requires an offline training stage in which the network learns the irradiance-to-GMPP voltage mapping from a pre-generated dataset (Section 4.1). Consequently, although PSO-MPPT measures the power of the array at runtime and needs no training, its search is restricted to the clusters identified offline (Section 3.3), so it also depends on prior knowledge of the array: under uniform irradiance of 900 W/m^2, whose single peak (about 65 V) lies between the original three candidates, it stayed at 45.5–50 V with 15–18% less power until a fourth candidate was added (Section 4.7). ANN-MPPT's accuracy, in turn, is inherently bounded by how representative the training dataset is of the shading conditions actually encountered in the field. This is in line with previous studies that have proposed metaheuristic [20–22], and ANN-based MPPT [27–30] strategies as a means of improving tracking performance under partial shading. This distinction is relevant because it allowed the impact of MPPT performance to be quantified not only in electrical terms (tracking error, converter efficiency) but also in terms of the ultimate deliverable of the system: pumped water volume.

An additional finding that, to the best of our knowledge, has received limited attention in the MPPT literature is the trade-off observed between GMPP tracking accuracy and overall efficiency (Section 4.6). The overall PV-to-hydraulic efficiency was highest (60.4%) precisely when IC-MPPT was trapped at the LMPP, and lower (57.40% and 56.99%) when PSO-MPPT and ANN-MPPT correctly tracked the GMPP. The stage-by-stage analysis shows that this difference originates almost entirely in the DC–DC converter: its efficiency decreased from 84.25% to 80.11% and 79.52%, whereas the motor (about 96.5%) and pump (about 74.3%) efficiencies remained practically unchanged across the three algorithms. The converter therefore dominates the variation in the overall efficiency. This counterintuitive result is consistent with the fact that the GMPP voltage in this PV array configuration is systematically lower than the LMPP voltage, so the converter must handle a higher current at equivalent power levels, with greater conduction losses. This finding suggests that efficiency alone is an incomplete metric for evaluating MPPT performance under partial shading, and that the volume of water actually delivered, the quantity of practical interest in a water pumping application, should take precedence when comparing MPPT strategies for this specific use case. It also identifies the converter as the main target for improving the overall efficiency of PSO-MPPT and ANN-MPPT.

From a practical standpoint, the observed 6.5–7% increase in cumulative pumped volume over the 20 s window of five stepped scenarios, and 3.9–4.6% over the 60 s continuous profile (Section 4.7), with gains of up to 17–18% during persistent shading, suggests that, in regions with frequent partial shading—such as rural areas of the Ecuadorian coast where nearby vegetation, structures, or cloud cover can unevenly shade PV arrays—the adoption of PSO-based or ANN-based MPPT could translate into a meaningful improvement in water availability for irrigation or domestic use, without changes to the PV array, converter, or motor–pump hardware already installed. This is particularly relevant given the region's favorable but variable solar resource [8,9,70] and the socioeconomic importance of reliable water access for agricultural productivity discussed in the Introduction.

This potential gain must be weighed against the additional sensing required. PSO-MPPT needs three irradiance measurements ($G_1 - G_3$) in addition to V and I, and ANN-MPPT needs the three irradiance measurements alone (Table 8), whereas IC-MPPT operates with V and I only. Irradiance sensors add capital cost, cabling and periodic recalibration, and a drift in their calibration would propagate directly into the cluster selection of PSO-MPPT and the reference voltage estimated by ANN-MPPT. No economic analysis was

performed in this study, so the benefit of 4–7% more water in the evaluated window cannot be assumed to justify the added hardware in every installation. Lower-cost alternatives to pyranometers, such as reference PV cells or small calibrated PV modules, could supply G_1—G_3. Electrical-only global-search strategies avoid the irradiance sensors altogether, but at the price of periodic power interruptions during the scan.

Nevertheless, several limitations of the present study should be acknowledged. First, the ANN uses only the irradiance levels of the three PV groups as inputs, so it was trained at a cell temperature of 25 °C. As shown in Section 4.8, a higher cell temperature shifts the GMPP voltage and degrades the ANN-MPPT, and to a lesser extent PSO-MPPT, unless compensation based on a module-temperature measurement is applied. Second, the training dataset was generated exclusively from simulated data obtained through a controlled voltage sweep of the PV array model; validation against experimental irradiance and power measurements from a physical PV array would strengthen confidence in the generalizability of the trained network beyond the simulated environment. Third, the dynamic comparison was carried out over a 20 s window of five discrete irradiance steps and a 60 s continuous profile with shading events (Section 4.7); although these allow a controlled, reproducible comparison, they do not capture the cumulative effect of MPPT performance over realistic diurnal irradiance profiles, which would be needed to quantify daily or seasonal water production gains. Fourth, as noted in Section 4.6, the stochastic nature of the PSO-MPPT search procedure was not characterized across multiple independent runs in this study; run-to-run variability in tracking error and cumulative volume remains to be quantified. Fifth, the same irradiance triplet is applied to all four parallel strings, so independent shading of each string or module was not evaluated. Because the voltage clusters used by PSO-MPPT and the training of ANN-MPPT depend on the bypass-diode structure and on how the irradiance is grouped, both would have to be re-identified and re-trained for other array configurations or shading structures. Moreover, the cluster-based PSO-MPPT can fail under conditions not represented by its candidates: in the 60 s run, the original three candidates did not include the single peak of uniform irradiance at 900 W/m^2, and a fourth candidate had to be added; other conditions outside the identified clusters could expose similar limitations. Sixth, the ANN was trained and tested on irradiance levels drawn from a discrete set between 200 and 1000 W/m^2, so its behavior for other levels, in particular below 200 W/m^2, was not evaluated, and neither was its sensitivity to noise or calibration errors in the irradiance measurements. Seventh, the temperature analysis was carried out offline on static P–V curves and not in the dynamic simulation, and the proposed compensation requires a module-temperature sensor; the noise of that sensor, the dependence of the voltage shift on the cluster and the temperature changes during operation were not evaluated.

Future work should therefore focus on: (i) validating the proposed PSO-based and ANN-based MPPT strategies against experimental data from a physical PV array under real partial shading conditions; (ii) incorporating cell temperature as an additional input of the ANN, as an alternative to the compensation proposed in Section 4.8, and validating that compensation in the dynamic simulation with a realistic temperature sensor; (iii) evaluating system performance over extended time horizons using realistic diurnal and seasonal irradiance profiles representative of the Ecuadorian coast, in order to quantify long-term gains in water delivery; (iv) characterizing the run-to-run variability of the PSO-MPPT algorithm across multiple independent simulations; (v) quantifying the cost–benefit of the irradiance sensing required by PSO-MPPT and ANN-MPPT and evaluating sensor-less or reduced-sensor alternatives; (vi) evaluating independent irradiance on each parallel string or module, which would change the number and position of the peaks; and (vii) benchmarking the proposed strategies against other advanced MPPT techniques

reported in the literature, such as additional metaheuristic [71,72] or hybrid strategies [30,73,74], and metaheuristic tuning of the controllers [75,76], under an equivalent evaluation framework.

6. Conclusions

This study evaluated three MPPT strategies, conventional IC-MPPT, PSO-MPPT exploiting GMPP voltage clusters, and ANN-MPPT estimating the GMPP voltage from irradiance, within a complete electromechanical–hydraulic model of a photovoltaic water pumping system under partial shading. Under pronounced shading, IC-MPPT converged to a local maximum in three of the five scenarios (mean tracking error 20.45%), whereas PSO-MPPT and ANN-MPPT tracked the GMPP in all scenarios (0.65% and 1.14%) and delivered approximately 6.5% and 7.0% more water in the evaluated 20 s window, and 3.9% and 4.6% more in a 60 s continuous irradiance profile. This gain came with a lower converter efficiency (84.25% for IC-MPPT against 80.11% and 79.52%), while the motor and pump efficiencies remained practically unchanged.

The two intelligent strategies performed comparably but differ in sensing (PSO-MPPT needs V, I and three irradiance measurements; ANN-MPPT needs the irradiance measurements only) and in implementation (runtime search versus offline-trained mapping), which should guide the choice for a given installation. Both rely on information obtained at a cell temperature of 25 °C; a higher temperature shifts the GMPP voltage and degrades ANN-MPPT more than PSO-MPPT, although a compensation based on a single module-temperature measurement recovers most of the loss. These results were obtained in simulation; future work includes experimental validation, a dynamic evaluation of the temperature compensation, and evaluation under realistic diurnal irradiance profiles to quantify long-term water production gains.

Author Contributions: Conceptualization, R.J.A.-C. and J.A.P.-R.; methodology, R.J.A.-C. and J.A.P.-R.; software, R.J.A.-C. and V.J.P.-B.; validation, R.J.A.-C., C.D.A.-J., Y.J.Z.-Z. and J.A.R.-M.; formal analysis, R.J.A.-C., J.A.P.-R. and C.D.A.-J.; investigation, R.J.A.-C., J.A.P.-R., V.J.P.-B., C.D.A.-J., Y.J.Z.-Z., J.E.N.-S., J.A.R.-M. and C.G.R.-B.; writing—original draft preparation, R.J.A.-C. and J.A.R.-M.; writing—review and editing, J.E.N.-S. and C.G.R.-B.; visualization, R.J.A.-C., Y.J.Z.-Z., J.E.N.-S. and C.G.R.-B.; supervision, J.A.P.-R.; project administration, R.J.A.-C. and V.J.P.-B. All authors have read and agreed to the published version of the manuscript.

Funding: This research was funded by the research project "Automatización de procesos operativos como estrategia para contribuir con la certificación Punto Verde de la ESPAM MFL", (Unique Project Code, CUP: 91880000.0000.390828), conducted by the INIAC research group of the Escuela Superior Politécnica Agropecuaria de Manabí Manuel Félix López (ESPAM MFL). Additional support was provided by the interinstitutional cooperation research project "Investigación y desarrollo de tecnologías inteligentes para la optimización de sistemas energéticos en el Ecuador," jointly conducted by the INIAC research group of ESPAM MFL and the ISII research group of the Universidad Técnica de Manabí (UTM). The APC was partially funded by ESPAM MFL.

Data Availability Statement: The data supporting the results of this study, including the simulation results and the dataset of 1000 irradiance scenarios used to train the ANN-MPPT algorithm, are available from the corresponding author upon reasonable request.

Acknowledgments: The authors would like to thank the Escuela Superior Politécnica Agropecuaria de Manabí Manuel Félix López (ESPAM MFL), the Universidad Técnica de Manabí (UTM), and the INIAC and ISII research groups for their academic, technical, and institutional support throughout the development of this research. During the preparation of this manuscript, the authors used ChatGPT (free version, OpenAI) and Claude (Sonnet 5.5, Anthropic) for the purposes of language editing, text refinement, and improving the clarity of the manuscript's structure. The authors have reviewed and edited the output and take full responsibility for the content of this publication.

Conflicts of Interest: The authors declare no conflicts of interest. The funders had no role in the design of the study; in the collection, analyses, or interpretation of data; in the writing of the manuscript; or in the decision to publish the results.

Abbreviations

The following abbreviations are used in this manuscript:

ANN	Artificial Neural Network
CCM	Continuous Conduction Mode
DCM	Discontinuous Conduction Mode
GMPP	Global Maximum Power Point
IC	Incremental Conductance
LMPP	Local Maximum Power Point
MPP	Maximum Power Point
MPPT	Maximum Power Point Tracking
PI	Proportional-Integral
PMDC	Permanent Magnet Direct Current
P&O	Perturb and Observe
PSO	Particle Swarm Optimization
PV	Photovoltaic
PVSWPS	Photovoltaic Solar Water Pumping Systems

References

1. Chadge, R.; Giri, J.; Amir, M.; Ilahi Bakhsh, F.; Sunheriya, N.; Mahatme, C.; Sathish, T. Investigation of Electrical Configuration Topologies for Enhancing the Performance of Solar Photovoltaic Water Pumping System. *Electr. Power Compon. Syst.* **2025**, *53*, 905–920. [CrossRef]
2. Cuenca, A.; Oña, C.; Suquillo, I.; Miniguano, H. Design Methodology of Off-Grid PV Solar Powered Systems for Rural Areas in Ecuador. *Rev. Téc. Energ.* **2023**, *20*, 43–51. [CrossRef]
3. Gevorkov, L.; Domínguez-García, J.L.; Romero, L.T. Review on solar photovoltaic-powered pumping Systems. *Energies* **2023**, *16*, 94. [CrossRef]
4. Andrade-Cedeno, R.J.; Pinargote-Bravo, V.J.; Amaya-Jaramillo, C.D.; Palacios-López, L.A.; Loor-Vera, A.T.; Pérez-Rodríguez, J.A.; Rodríguez-Borges, C.G. A sustainable and efficient alternative for water pumping in electrically isolated rural areas of Ecuador. *Energy Rep.* **2023**, *10*, 719–733. [CrossRef]
5. García-Guillén, A.; Gutiérrez-Hinestroza, M.; Moreno-Alcívar, L.; Bravo-Montero, L.; Herrera-Franco, G. Photovoltaic System for Residential Energy Sustainability in Santa Elena, Ecuador. *Environments* **2025**, *12*, 281. [CrossRef]
6. Sontake, V.C.; Kalamkar, V.R. Solar photovoltaic water pumping system—A comprehensive review. *Renew. Sustain. Energy Rev.* **2016**, *59*, 1038–1067. [CrossRef]
7. Shepovalova, O.V.; Belenov, A.T.; Chirkov, S.V. Review of photovoltaic water pumping system research. *Energy Rep.* **2020**, *6*, 306–324. [CrossRef]
8. Echegaray-Aveiga, R.C.; Masabanda, M.; Rodríguez, F.; Toulkeridis, T.; Mato, F. Solar energy potential in Ecuador. In *Proceedings of the 2018 International Conference on eDemocracy & eGovernment (ICEDEG)*; IEEE: New York, NY, USA, 2018; pp. 46–51. [CrossRef]
9. Romero Paguay, J.A.; Sancho Aguilera, D.; Inca Guamán, A.V.; Loján Carrión, M.D.C. Implementación de Sistema Solar Fotovoltaico: Evaluación de Sostenibilidad y Eficiencia Energética. *Rev. Veritas Difus. Científica* **2024**, *5*, 1745–1767. [CrossRef]
10. Hilali, A.; Mardoude, Y.; Essahlaoui, A.; Rahali, A.; Ouanjli, N.E. Migration to solar water pump system: Environmental and economic benefits and their optimization using genetic algorithm Based MPPT. *Energy Rep.* **2022**, *8*, 10144–10153. [CrossRef]
11. Fan, Z.; Li, S.; Cheng, H.; Liu, L. Perturb and Observe MPPT Algorithm of photovoltaic System: A Review. In *Proceedings of the 2021 33rd Chinese Control and Decision Conference (CCDC)*; IEEE: New York, NY, USA, 2021; pp. 1413–1418. [CrossRef]
12. Mahdhi, H.B.; Moujahed, M.; Slimene, M.B.; Khlifi, M.A.; Benazza, H. Performance analysis of MPPT techniques in a PV-powered water pumping system using an induction motor. *Sci. Rep.* **2026**, *16*, 21702. [CrossRef] [PubMed]
13. Pant, S.; Saini, R.P. Solar water pumping system modelling and analysis using MATLAB/Simulink. In *Proceedings of the 2020 IEEE Students Conference on Engineering & Systems (SCES)*; IEEE: New York, NY, USA, 2020; pp. 1–6. [CrossRef]
14. Amal, Z. Advanced Perturb and Observe Algorithm for Maximum Power Point Tracking in Photovoltaic Systems with Adaptive Step Size. *J. Autom. Mob. Robot. Intell. Syst.* **2024**, *18*, 55–60. [CrossRef]
15. Sakhri, Z.; Bekkour, E.-H.; Mahfoud, S.; Bossoufi, B.; Skruch, P.; Mobayen, S. Real-time simulation, implementation, and new structure of DTC for a photovoltaic water pumping system based on a DFIM. *Energy* **2026**, *12*, 100670. [CrossRef]

16. Seba, S.; Mouhoub, B.; Benmouiza, K. A Comparative Analysis of series and parallel topologies of Perturb and Observe (P&O) and Incremental Conductance (InC) MPPT Algorithms for Photovoltaic System. *Alger. J. Renew. Energy Sustain. Dev.* **2023**, *5*, 11–21. [CrossRef]
17. Lemmassi, A.; Derouich, A.; Hanafi, A.; Byou, A.; Benmessaoud, M.; El Ouanjli, N. Low-cost MPPT for triple-junction solar cells used in nanosatellites: A comparative study between P&O and INC algorithms. *E-Prime-Adv. Electr. Eng. Electron. Energy* **2024**, *7*, 100426. [CrossRef]
18. Bendib, D.; Laour, M. Modified incremental conductance MPPT using SEPIC converter for PV system, simulation and arduino implementation. *Stud. Eng. Exact Sci.* **2024**, *5*, e6614. [CrossRef]
19. Li, C.; Chen, Y.; Zhou, D.; Liu, J.; Zeng, J. A High-Performance Adaptive Incremental Conductance MPPT Algorithm for Photovoltaic Systems. *Energies* **2016**, *9*, 288. [CrossRef]
20. Li, J.; Wu, Y.; Ma, S.; Chen, M.; Zhang, B.; Jiang, B. Analysis of photovoltaic array maximum power point tracking under uniform environment and partial shading condition: A review. *Energy Rep.* **2022**, *8*, 13235–13252. [CrossRef]
21. Chellakhi, A.; El Beid, S.; Marghichi, M.E.; Bouabdalli, E.M. An amended low-cost indirect MPPT strategy with a PID controller for boosting PV system efficiency. *Results Eng.* **2024**, *24*, 103526. [CrossRef]
22. Ali, A.I.M.; Mousa, H.H.H.; Mohamed, H.R.A.; Kamel, S.; Hassan, A.S.; Alaas, Z.M.; Mohamed, E.E.M.; Abdallah, A.-R.Y. An Enhanced P&O MPPT Algorithm with Concise Search Area for Grid-Tied PV Systems. *IEEE Access* **2023**, *11*, 79408–79421. [CrossRef]
23. Al-Muthanna, G.; Fang, S.; AL-Wesabi, I.; Ameur, K.; Kotb, H.; AboRas, K.M.; Garni, H.Z.A.; Mas'ud, A.A. A High Speed MPPT Control Utilizing a Hybrid PSO-PID Controller under Partially Shaded Photovoltaic Battery Chargers. *Sustainability* **2023**, *15*, 3578. [CrossRef]
24. Priyadarshi, N.; Bhaskar, M.S.; Padmanaban, S.; Blaabjerg, F.; Azam, F. New CUK–SEPIC converter based photovoltaic power system with hybrid GSA–PSO algorithm employing MPPT for water pumping applications. *IET Power Electron.* **2020**, *13*, 2824–2830. [CrossRef]
25. Al-Majidi, S.D.; Abbod, M.F.; Al-Raweshidy, H.S. A particle swarm optimisation-trained feedforward neural network for predicting the maximum power point of a photovoltaic array. *Eng. Appl. Artif. Intell.* **2020**, *92*, 103688. [CrossRef]
26. Magalhães, B.; Pombo, J.; Mendes, W.; Calado, M.; Mariano, S.; Louro, M. A Review of Particle Swarm Optimization Control Parameters for Maximum Power Point Tracking Under Different Conditions. *Sustainability* **2026**, *18*, 5442. [CrossRef]
27. Abdallah, F.S.M.; Abdullah, M.N.; Musirin, I.; Elshamy, A.M. Intelligent solar panel monitoring system and shading detection using artificial neural networks. *Energy Rep.* **2023**, *9*, 324–334. [CrossRef]
28. BalaKumar, S.; Lemma, M.; Godato, M. Solar-powered ANN-based MPPT with zeta converter for BLDC motor water pumping in rural Ethiopia for sustainable agriculture. *Discov. Sustain.* **2025**, *6*, 140. [CrossRef]
29. Villegas-Mier, C.G.; Rodriguez-Resendiz, J.; Álvarez-Alvarado, J.M.; Rodriguez-Resendiz, H.; Herrera-Navarro, A.M.; Rodríguez-Abreo, O. Artificial neural networks in MPPT algorithms for optimization of photovoltaic power systems: A review. *Micromachines* **2021**, *12*, 1260. [CrossRef] [PubMed]
30. Guerra, M.I.S.; Ugulino De Araújo, F.M.; Dhimish, M.; Vieira, R.G. Assessing Maximum Power Point Tracking Intelligent Techniques on a PV System with a Buck–Boost Converter. *Energies* **2021**, *14*, 7453. [CrossRef]
31. Andrade-Cedeno, R.J.; Pérez-Rodríguez, J.A.; Amaya-Jaramillo, C.D.; Rodríguez-Borges, C.G.; Vera-Cedeno, E.R.; Quiroz-Fernández, L.S.; Llosas-Albuerne, Y.E. Comparative study by numerical simulation of two methods for automatic flow control in centrifugal pumps. *Int. J. Power Electron. Drive Syst. IJPEDS* **2022**, *13*, 1365. [CrossRef]
32. Yussif, N.; Sabry, O.H.; Abdel-Khalik, A.S.; Ahmed, S.; Mohamed, A.M. Enhanced Quadratic V/f-Based Induction Motor Control of Solar Water Pumping System. *Energies* **2020**, *14*, 104. [CrossRef]
33. Farhat, M.; Barambones, O. Advanced Control Scheme Optimization for Stand-Alone Photovoltaic Water Pumping Systems. *Computation* **2024**, *12*, 224. [CrossRef]
34. Nisha, R.; Gnana Sheela, K. Metaheuristic Algorithm Based Maximum Power Point Tracking Technique Combined with One Cycle Control for Solar Photovoltaic Water Pumping Systems. *Front. Energy Res.* **2022**, *10*, 902443. [CrossRef]
35. Khadija, S.; Ouadia, E.M.; Abdelmajid, F. Tracking the GMPP of a solar photovoltaic water pumping system with an SMC controller in partial shading conditions. *Bull. Electr. Eng. Inform.* **2023**, *12*, 3298–3310. [CrossRef]
36. Merbah, A.; Tadjer, S.A. Evaluation of metaheuristic tracking methods in photovoltaic water pumping under partial shading. *Rev. Roum. Sci. Tech.—Sér. Électrotechnique Énergétique* **2026**, *71*, 349–354. [CrossRef]
37. Bouselham, L.; Hajji, M.; Hajji, B.; Bouali, H. A MPPT-based ANN controller applied to PV pumping system. In *Proceedings of the 2016 International Renewable and Sustainable Energy Conference (IRSEC)*; IEEE: New York, NY, USA, 2016; pp. 86–92. [CrossRef]
38. Hayder, W.; Sera, D.; Ogliari, E.; Lashab, A. On Improved PSO and Neural Network P&O Methods for PV System under Shading and Various Atmospheric Conditions. *Energies* **2022**, *15*, 7668. [CrossRef]

39. Cruz, B.; Ricalde, L.; Quintal-Palomo, R.; Bassam, A.; Rico-Camacho, R.I. Hybrid Artificial Neural Network and Perturb & Observe Strategy for Adaptive Maximum Power Point Tracking in Partially Shaded Photovoltaic Systems. *Energies* **2025**, *18*, 5053. [CrossRef]
40. Green, M.A.; Emery, K.; Hishikawa, Y.; Warta, W.; Dunlop, E.D. Solar cell efficiency tables (version 48). *Prog. Photovolt. Res. Appl.* **2016**, *24*, 905–913. [CrossRef]
41. Ishaque, K.; Salam, Z.; Syafaruddin. A comprehensive MATLAB Simulink PV system simulator with partial shading capability based on two-diode model. *Sol. Energy* **2011**, *85*, 2217–2227. [CrossRef]
42. Jannat, N.; Mishu, S.N.; Pallab, P.B.; Nishat, M.A.H.; Ahmed, M.F.; Kabir, M.H. Double-Diode Modeling and Simulation of PV Cell Performance: Statistical Analysis and Machine-Learning Validation. *Lights* **2026**, *2*, 7. [CrossRef]
43. Ishaque, K.; Salam, Z.; Taheri, H. Accurate MATLAB Simulink PV System Simulator Based on a Two-Diode Model. *J. Power Electron.* **2011**, *11*, 179–187. [CrossRef]
44. Kumari, N.; Singh, S.K.; Kumar, S. A Review on Performance and Reliability Aspects of Photovoltaic Modules. In *Sustainable Technology and Advanced Computing in Electrical Engineering*; Mahajan, V., Chowdhury, A., Padhy, N.P., Lezama, F., Eds.; Lecture Notes in Electrical Engineering; Springer Nature: Singapore, 2022; Volume 939, pp. 589–601. [CrossRef]
45. Alimi, O.A.; Meyer, E.L.; Olayiwola, O.I. Solar Photovoltaic Modules' Performance Reliability and Degradation Analysis—A Review. *Energies* **2022**, *15*, 5964. [CrossRef]
46. Magheț, A.-E.; Ilie, S.; Toader, D. The Numerical Model of a PV System Supported by Experimental Validation. *Appl. Sci.* **2026**, *16*, 1891. [CrossRef]
47. Ait Ayad, I.; Elwarraki, E.; Baghdadi, M. Intelligent Perturb and Observe Based MPPT Approach Using Multilevel DC-DC Converter to Improve PV Production System. *J. Electr. Comput. Eng.* **2021**, *2021*, 6673022. [CrossRef]
48. Divyasharon, R.; Banu, R.N.; Devaraj, D. Artificial neural network based MPPT with Cuk converter topology for PV systems under varying climatic conditions. In *Proceedings of the 2019 IEEE International Conference on Intelligent Techniques in Control, Optimization and Signal Processing (INCOS)*; IEEE: New York, NY, USA, 2019; pp. 1–6. [CrossRef]
49. Seguel, J.L.; Seleme, S.I.; Morais, L.M.F. Comparative Study of Buck-Boost, SEPIC, Cuk and Zeta DC-DC Converters Using Different MPPT Methods for Photovoltaic Applications. *Energies* **2022**, *15*, 7936. [CrossRef]
50. Assidiq, A.R.; Dahono, A.; Rizqiawan, A.; Furqani, J. High ratio DC-DC converter based on cascade modified Cuk converter topology. *E-Prime-Adv. Electr. Eng. Electron. Energy* **2024**, *9*, 100654. [CrossRef]
51. Muñoz-Galeano, N.; López-Lezama, J.M.; Cano-Quintero, J.B. Modelling of hybrid Cuk converters using the methodology of voltage and current references. *Rev. UIS Ing.* **2022**, *21*, 53–62. [CrossRef]
52. Id Ouissaaden, F.; Kamel, H.; Dlimi, S. Simulation and Performance Evaluation of a Photovoltaic Water Pumping System with Hybrid Maximum Power Point Technique (MPPT) for Remote Rural Areas. *Processes* **2025**, *13*, 2867. [CrossRef]
53. Hadimani S, C.; Raju, A.B.; Radha, R.; Jyoti, R. Photovoltaic based PMDC motor drive system using MPPT. In *Proceedings of the 2016 Second International Conference on Cognitive Computing and Information Processing (CCIP)*; IEEE: New York, NY, USA, 2016; pp. 1–6. [CrossRef]
54. Mohammad, K.; Ahmad, M.; Farooqui, S.A.; Ali, W.; Khan, F. Performance evaluation of a PMDC motor with battery storage control and MPPT based solar photovoltaic system. *Int. J. Power Electron. Drive Syst. IJPEDS* **2022**, *13*, 1704. [CrossRef]
55. Harrouz, A.; Becheri, H.; Colak, I.; Kayisli, K. Backstepping control of a separately excited DC motor. *Electr. Eng.* **2018**, *100*, 1393–1403. [CrossRef]
56. Andrade-Cedeno, R.J.; Pérez-Rodríguez, J.A.; Amaya-Jaramillo, C.D.; Rodríguez-Borges, C.G.; Llosas-Albuerne, Y.E.; Barros-Enríquez, J.D. Numerical study of constant pressure systems with variable speed electric pumps. *Energies* **2022**, *15*, 1918. [CrossRef]
57. Moubarak, A.; El-Saady, G.; Ibrahim, E.-N.A. Variable speed photovoltaic water pumping using affinity laws. *J. Power Energy Eng.* **2017**, *5*, 50–71. [CrossRef]
58. Simpson, A.R.; Marchi, A. Evaluating the Approximation of the Affinity Laws and Improving the Efficiency Estimate for Variable Speed Pumps. *J. Hydraul. Eng.* **2013**, *139*, 1314–1317. [CrossRef]
59. Bava, F.; Dragsted, J.; Furbo, S. A numerical model to evaluate the flow distribution in a large solar collector field. *Sol. Energy* **2017**, *143*, 31–42. [CrossRef]
60. Ashok Kumar, B.; Srinivasa Venkatesh, M.; Mohan Muralikrishna, G. Optimization of Photovoltaic Power Using PID MPPT Controller Based on Incremental Conductance Algorithm. In *Power Electronics and Renewable Energy Systems*; Kamalakannan, C., Suresh, L.P., Dash, S.S., Panigrahi, B.K., Eds.; Lecture Notes in Electrical Engineering; Springer: New Delhi, India, 2015; Volume 326, pp. 803–809. [CrossRef]
61. Elobaid, L.M.; Abdelsalam, A.K.; Zakzouk, E.E. Artificial neural network-based photovoltaic maximum power point tracking techniques: A survey. *IET Renew. Power Gener.* **2015**, *9*, 1043–1063. [CrossRef]

62. Roy, R.B.; Rokonuzzaman, M.; Amin, N.; Mishu, M.K.; Alahakoon, S.; Rahman, S.; Mithulananthan, N.; Rahman, K.S.; Shakeri, M.; Pasupuleti, J. A Comparative Performance Analysis of ANN Algorithms for MPPT Energy Harvesting in Solar PV System. *IEEE Access* **2021**, *9*, 102137–102152. [CrossRef]
63. Podrzaj, P. Contionuous VS discrete PID controller. In *Proceedings of the 2018 IEEE 9th International Conference on Mechanical and Intelligent Manufacturing Technologies (ICMIMT)*; IEEE: New York, NY, USA, 2018; pp. 177–181. [CrossRef]
64. Mao, M.; Cui, L.; Zhang, Q.; Guo, K.; Zhou, L.; Huang, H. Classification and summarization of solar photovoltaic MPPT techniques: A review based on traditional and intelligent control strategies. *Energy Rep.* **2020**, *6*, 1312–1327. [CrossRef]
65. Kumari, P.; Dang, A.; Mahto, U.; Kumar, R. Design and Implementation of P&O MPPT algorithm for Solar PV System. *Int. J. Sci. Res. Eng. Manag.* **2025**, *9*, 1–9. [CrossRef]
66. Mohamed, S.A.; Abd El Sattar, M. A comparative study of P&O and INC maximum power point tracking techniques for grid-connected PV systems. *SN Appl. Sci.* **2019**, *1*, 174. [CrossRef]
67. Ruchira; Patel, R.N.; Sinha, S.K. Comparison of ANN-based MPPT controller and incremental conductance for photovoltaic system. In *Proceeding of the Second International Conference on Microelectronics, Computing & Communication Systems (MCCS 2017)*; Nath, V., Mandal, J.K., Eds.; Springer: Singapore, 2019; pp. 295–305. [CrossRef]
68. Bollipo, R.B.; Mikkili, S.; Bonthagorla, P.K. Hybrid, optimal, intelligent and classical PV MPPT techniques: A review. *CSEE J. Power Energy Syst.* **2021**, *7*, 9–33. [CrossRef]
69. Shukla, A.; Titare, L.S. An Efficient Neural Network-based MPPT technique for PV Array Under Partial Shading Conditions. In *Proceedings of the 2021 International Conference on Smart Generation Computing, Communication and Networking (SMART GENCON)*; IEEE: New York, NY, USA, 2021; pp. 1–5. [CrossRef]
70. Espinoza Echeverría, S.; Guayanlema, V. *Balance y Proyecciones del Sistema de Subsidios Energéticos en Ecuador*; Friedrich Ebert Stiftung: Quito, Ecuador, 2017; Available online: http://library.fes.de/pdf-files/bueros/quito/13648.pdf.
71. Rong, J.; Li, S.; Xiang, S. Research on Maximum Power Point Tracking Based on an Improved Harris Hawks Optimization Algorithm. *Electronics* **2025**, *14*, 2157. [CrossRef]
72. Silaa, M.Y.; Barambones, O.; Bencherif, A.; Rahmani, A. A New MPPT-Based Extended Grey Wolf Optimizer for Stand-Alone PV System: A Performance Evaluation versus Four Smart MPPT Techniques in Diverse Scenarios. *Inventions* **2023**, *8*, 142. [CrossRef]
73. Boutabba, T.; Drid, S.; Chrifi-Alaoui, L. Experimental control of photovoltaic system using neuro—Kalman filter maximum power point tracking (MPPT) technique. *Int. J. Emerg. Electr. Power Syst.* **2020**, *21*, 20190210. [CrossRef]
74. Garud, K.S.; Jayaraj, S.; Lee, M. A review on modeling of solar photovoltaic systems using artificial neural networks, fuzzy logic, genetic algorithm and hybrid models. *Int. J. Energy Res.* **2021**, *45*, 6–35. [CrossRef]
75. Zafar, M.H.; Mansoor, M.; Khan, N.M.; Sanfilippo, F. Optimal Tuning of PID Controller for Boost Converter using Meta-Heuristic Algorithm for Renewable Energy Applications. In *ICMAME 2023 Conference Proceedings*; ECER: Dubai, United Arab Emirates, 2023. [CrossRef]
76. Kechida, R.; Gacem, A.; Romdhane, M.; Naoui, M.; Almalaq, Y.; Alturki, M.; Albaker, A.; Guesmi, T. High-efficiency predictive torque control of induction motors in PV water pumping using GTO-optimized PI controller. *Sci. Rep.* **2026**, *16*, 13428. [CrossRef] [PubMed]

Disclaimer/Publisher's Note: The statements, opinions and data contained in all publications are solely those of the individual author(s) and contributor(s) and not of MDPI and/or the editor(s). MDPI and/or the editor(s) disclaim responsibility for any injury to people or property resulting from any ideas, methods, instructions or products referred to in the content.